p-wave superconductivity and Josephson current in *p*-wave unconventional magnet/*s*-wave superconductor hybrid systems

Yuri Fukaya,[1] Keiji Yada,[2] and Yukio Tanaka[2]
[1]*Faculty of Environmental Life, Natural Science and Technology, Okayama University, Okayama 700-8530, Japan*
[2]*Department of Applied Physics, Nagoya University, Nagoya 464-8603, Japan*

(Received 29 December 2025; revised 7 June 2026; accepted 12 June 2026; published 6 July 2026)

We study the surface density of states in *p*-wave unconventional magnet/spin-singlet *s*-wave superconductor hybrid systems (*p*-wave unconventional magnetic superconductors). Owing to the noncollinear spin structure in *p*-wave unconventional magnets, the spin-singlet *s*-wave pair potential behaves as the spin-triplet *p*-wave superconductivity. As a result, zero-energy flat bands can emerge at the edge. Analyzing the pair amplitude at the edge, odd-frequency spin-triplet even-parity pairing is induced in the presence of zero-energy flat bands, while even-frequency spin-singlet even parity remains. We also demonstrate the Josephson current in superconducting junctions with *p*-wave unconventional magnet/spin-singlet *s*-wave superconductor hybrid systems. By the cooperation of the spin-singlet *s*-wave pair potential and the *p*-wave unconventional magnetic order, the coupling of the spin-singlet even-parity pairings in junctions generates the first harmonics of the Josephson current. In addition, the temperature dependence of the maximum Josephson current can be tuned by the chemical potential, which determines the generation of zero-energy flat bands. Our results indicate that the $s + p$-wave-like superconducting state is generated in *p*-wave unconventional magnet/*s*-wave superconductor hybrid systems.

DOI: 10.1103/2gh7-y6w5

I. INTRODUCTION

The search for topological superconductivity [1–7] plays an important role in the emergence of quantum computing for Majorana zero modes [8–11] characterized by zero-energy flat bands, which are topologically protected by winding numbers [3,12–17] and are relevant to odd-frequency superconductivity [7]. In particular, it is known that spin-triplet p_x-wave pairing leads to Majorana zero modes at the edge in one-dimensional superconductors (SCs) of the Kitaev chain model [18]; however, spin-triplet *p*-wave SCs are not in general favorable in realistic materials. For this perspective, a nanowire model, etc., with conventional *s*-wave SCs has been proposed [19–24], and spin-triplet p_x-wave pairing is effectively induced to realize Majorana zero modes. Indeed, the realization of the Majorana zero modes and zero-energy flat bands can be achieved by reducing the degree of freedom of an electron, which is caused by ferromagnetism, magnetic spin structure like a spin helix, and so on [23,25,26], as well as by the proximity effect in superconducting junctions [27–34].

It is known that the charge transport properties in superconducting junctions are strongly influenced by the edge states and spin structures of SCs [13,17,35–41]. In particular, these configurations determine the behavior of the current phase relation in Josephson junctions [37,39]. For instance, in conventional spin-singlet *s*-wave SC/spin-singlet *s*-wave SC Josephson junctions, without any edge states, the current phase relation is generally described by $\sum_m I_m \sin(m\varphi)$ with $I_1 > 0$ and the phase difference φ. In the low-transparency limit studied by Ambegaokar and Baratoff, $I_1 \sin\varphi$ is satisfied, and the maximum Josephson current is saturated at low temperatures [42]. While in spin-triplet *p*-wave SC/spin-singlet *s*-wave SC junctions, because spin-triplet pairing cannot be coupled to spin-singlet pairing within the first order of the tunneling process, the I_1 component vanishes [43–50]. Besides, in p_x-wave SC/p_x-wave SC junctions, the Josephson current is enhanced by the resonance of zero-energy flat bands on both sides of the junctions [51–53]. However, in p_x-wave SC/p_y-wave SC junctions, the spin-triplet components cannot be mixed within the first order owing to the different parity symmetries in the mirror plane along the interface [51,52].

Recently, a new class of magnetism has been discovered as "altermagnetism" [55–70], as well as odd-parity unconventional magnetism [54,71,72]. In the former case, altermagnet/SC hybrid systems and superconducting junctions with altermagnetism exhibit Andreev reflection [73–76], anomalous transport properties [77–85], nonreciprocal supercurrent [86–92], as well as topological superconductivity [34,91,93–105], etc. [106–121]. In the latter case, *p*-wave unconventional magnetism is characterized by noncollinear spin structure [54,71,72] and the resulting Fermi surface has a *p*-wave-like spin splitting. As well as altermagnets, transport properties and so on in *p*-wave unconventional magnet (PUM)/SC systems have been studied [80,122–125]. Recently, some experiments have been successful in fabricating PUMs: NiI_2 [126] and $Gd_3(Ru_{(1-\delta)}Rh_\delta)_4Al_{12}$ [127].

Published by the American Physical Society under the terms of the Creative Commons Attribution 4.0 International license. Further distribution of this work must maintain attribution to the author(s) and the published article's title, journal citation, and DOI.

It is known that ferromagnet/SC hybrid systems are the main topic of superconducting spintronics [128] and topological superconductivity [1–7], etc. Apart from the ferromagnetism, because it is expected that unconventional magnetism does not break the superconductivity owing to the zero net magnetism, exotic superconducting phenomena can be led in hybrid systems with unconventional magnets and SCs. In fact, altermagnetism in hybrid systems leads to higher-order topological superconductivity [94–99], subgap states [129], and the crossed zero-energy flat bands [130]. Likewise, in hybrid systems with a PUM, possible topological superconductivity and the edge states are proposed [72,123,125,131–137]. In Ref. [123], they adopted the effective PUM model proposed in Ref. [71], and zero-energy flat bands can be exhibited by tuning the chemical potential and p-wave magnetic order. Indeed, studying hybrid systems composed of an unconventional magnet and SC is applicable for observing signatures of zero-energy flat bands in the tunneling spectroscopy experimentally. Thus, it is timely to study not only charge transport behaviors but also pairing symmetry of hybrid systems with an unconventional magnet and SC.

In this work, we demonstrate the emergence of p-wave superconductivity in PUM-spin-singlet s-wave SC hybrid systems: p-wave unconventional magnetic superconductors (PUM-SCs), by using the distinct PUM model [54]. We show that zero-energy flat bands, which can be relevant to Majorana zero modes, can exhibit at the [100] edge owing to the noncollinear spin structure in the zx plane, as also worked in Ref. [123]. Then p-wave unconventional magnetic order leads to p-wave superconductivity associated with the spin-dependent hopping. We analyze the pair amplitude at the [100] edge, and odd-frequency spin-triplet even-parity pairing can be realized in the presence of zero-energy flat bands, while even-frequency spin-singlet even-parity pairing also remains at the edge. We also study the Josephson current in superconducting junctions with PUM-SCs along the x direction. Because the spin-singlet even-parity pair amplitude exhibits in PUM-SCs, the coupling of spin-singlet even-parity pairings on both sides of the junctions can occur and affect the current phase relation of the Josephson current. Our results propose a more realistic implementation of zero-energy flat bands and the Josephson current, and broaden the possible methodology of the realization of spin-triplet p-wave superconductivity by the noncollinear spin structure of PUM.

The construction of this paper is as follows. In Sec. II, we provide the model Hamiltonian and the Fermi surface in PUM. We study the surface density of states (SDOS) at the edge in PUM-SCs in Sec. III and pair amplitude at the edge in Sec. IV. We also study the Josephson effect in the high-transparency limit in Sec. V. In Sec. VI, we show the temperature dependence of the maximum Josephson current in the low transparency limit. Finally, we summarize and conclude our work in Sec. VII.

II. MODEL HAMILTONIAN

First, we present the model Hamiltonian in PUM. The effective model of PUM has already been proposed in Refs. [54,71]. In this study, we deal with the tight-binding model suggested in Ref. [54]:

$$\hat{H}(\boldsymbol{k}) = \varepsilon(\boldsymbol{k})\hat{s}_0 \otimes \hat{\sigma}_0 + [t_x \sin k_x + t_y \sin k_y]\hat{s}_3 \otimes \hat{\sigma}_0 + J\hat{s}_1 \otimes \hat{\sigma}_3, \tag{1}$$

with the kinetic energy term $\varepsilon(\boldsymbol{k}) = -\mu - 2t\cos k_x - 2t\cos k_y$, the intrasector hopping t, the chemical potential μ, local sd interaction J, and the spin-dependent hopping t_x and t_y. Here, $\hat{s}_{0,1,2,3}$ and $\hat{\sigma}_{0,1,2,3}$ denote the Pauli matrices in spin and sector space, respectively. In the Supplemental Material of Ref. [54], the size of the original Hamiltonian in a minimal magnetic lattice is described as 8×8. In Eq. (1), the 4×4 Hamiltonian has been proposed to capture p-wave unconventional magnetism in the lattice model [Figs. 1(a) and 1(b)] [54]. In this model, t_x and t_y terms generate the spin-helix structure [27,32,138–145], and the additional J configuration leads to the noncollinear spin structure that characterizes p-wave unconventional magnetism shown in Figs. 1(a) and 1(b). Then, p_x (p_y)-wave magnetism is obtained by t_x (t_y) with nonzero J [54]. Equation (1) can be separated into two sectors:

$$\hat{H}^{\eta}(\boldsymbol{k}) = \varepsilon(\boldsymbol{k})\hat{s}_0 + [t_x \sin k_x + t_y \sin k_y]\hat{s}_3 + \eta J\hat{s}_1, \tag{2}$$

with the indices of the sector degrees of freedom $\eta = \pm1$, and the corresponding eigenvalues are given by

$$\bar{E}_{\pm} = \varepsilon(\boldsymbol{k}) \pm \sqrt{(t_x \sin k_x + t_y \sin k_y)^2 + J^2}. \tag{3}$$

We show the Fermi surface of PUM with the expectation value of $S_z = (\hbar/2)\hat{s}_z$ at $\mu = -4t, -2t$, and $(t_x, t_y) = (t, 0)$ and $(0, t)$ in Figs. 1(c)–1(f). These Fermi surfaces are doubly degenerate for each sector $\eta = \pm1$. When we choose the parameters as $(t_x, t_y) = (t, 0)$ shown in Figs. 1(c) ($\mu = -4t$) and 1(d) ($\mu = -2t$), we obtain the Fermi surface with p_x-wave unconventional magnetism, and then the numbers of Fermi surfaces are 1 and 2, respectively. Likewise, the Fermi surfaces with p_y-wave magnetism are demonstrated at $(t_x, t_y) = (0, t)$ [Fig. 1(e) for $\mu = -4t$ and Fig. 1(f) for $\mu = -2t$]. The obtained Fermi surface and the spin expectation values are the same as the result for p_x-wave UM cases with $\pi/2$ rotation. These demonstrations indicate that the direction of the noncollinear spin structure can be tuned by t_x and t_y terms. It is noted that the expectation value of $S_x = (\hbar/2)\hat{s}_x$ ($\langle S_x \rangle$) in the normal state is canceled because its sign is opposite in each sector.

Here, we introduce the Bogoliubov–de Gennes Hamiltonian for PUM/s-wave SC hybrid systems (PUM-SCs) shown in Figs. 2(a) and 3(a) in the bulk [111]:

$$\hat{H}_{\mathrm{BdG}}(\boldsymbol{k}) = \begin{pmatrix} \hat{H}(\boldsymbol{k}) & \hat{\Delta} \\ \hat{\Delta}^{\dagger} & -\hat{H}^{*}(-\boldsymbol{k}) \end{pmatrix}. \tag{4}$$

We assume the conventional intrasector spin-singlet s-wave pairing:

$$\hat{\Delta} = \Delta[\hat{s}_0 \otimes \hat{\sigma}_0]i\hat{s}_2 \tag{5}$$

where Δ is the magnitude of the pair potential. As topological superconductivity has been proposed in the nanowire model [19,20], magnetic chain [23,26], etc. [25], spin-singlet s-wave pairing has been adopted for the proximity. Based on these previous works and Ref. [146], we choose the spin-singlet s-wave pair potential in PUM-SC.

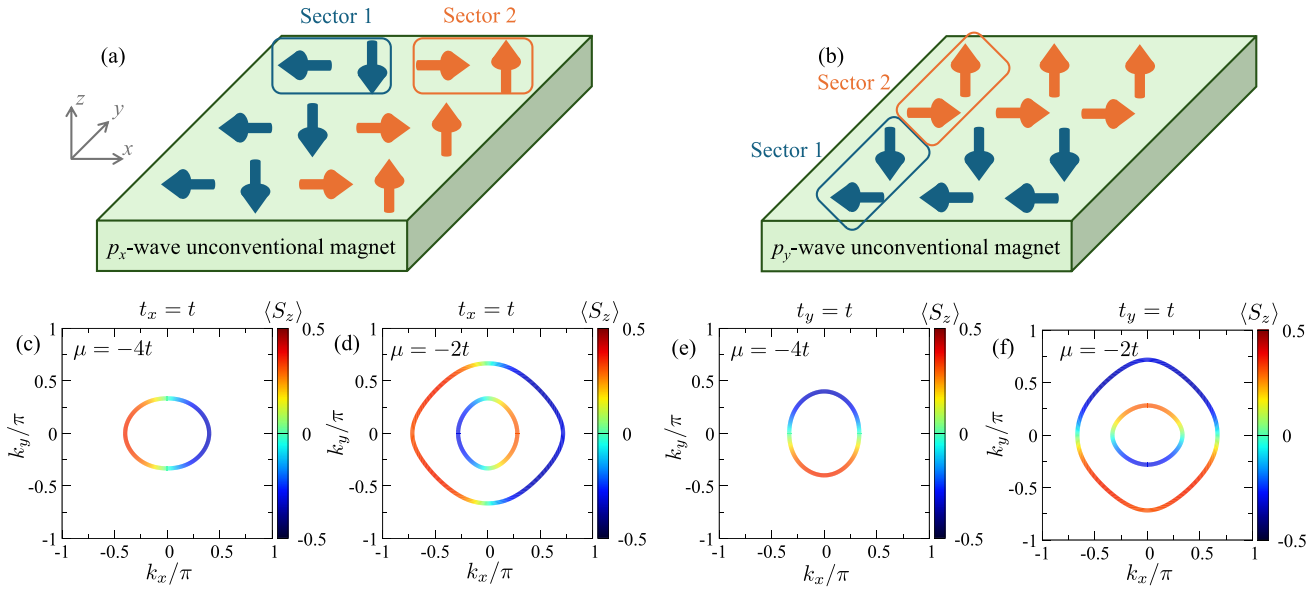


FIG. 1. (a), (b) Schematic illustration of the two-dimensional p-wave unconventional magnet (PUM) at (a) $t_x \neq 0$ ($t_y = 0$) and (b) $t_y \neq 0$ ($t_x = 0$) in Eq. (1). Arrows stand for the noncollinear spin structure in PUM, and blue and red colors indicate the combination of the sectors, suggested in Ref. [54]. In the effective Hamiltonian, two sectors (sectors 1 and 2) and spin degrees of freedom (up and down spins) contribute to the basis of the Hamiltonian [54]. Both $J = t$ and $t_{x,y}$ terms lead to the noncollinear spin structures of p-wave unconventional magnetism. (c)–(f) Fermi surface at (c) $(\mu, t_x, t_y) = (-4t, t, 0)$, (d) $(-2t, t, 0)$, (e) $(-4t, 0, t)$, and (f) $(-2t, 0, t)$. We set $J = t$ in panels (c)–(f).

III. SURFACE DENSITY OF STATES AT THE [100] EDGE

In this section, we discuss the p-wave superconductivity and the emergence of the edge states in PUM-SCs. For this purpose, we calculate the SDOS by using the retarded Green's function $\hat{G}^{\mathrm{R}}(k_y, z)$ for $z = E + i\delta$:

$$D(E) = \int_{-\pi}^{\pi} \rho(E, k_y) dk_y, \tag{6}$$

$$\rho(E, k_y) = -\frac{1}{\pi} \mathrm{Im} \mathrm{Tr}' \tilde{G}^{\mathrm{R}}(k_y, z), \tag{7}$$

with the energy E and the infinitesimal value $\delta = 0.01\Delta$. We adopt the recursive Green's function method to obtain the semi-infinite Green's function $\tilde{G}^{\mathrm{R}}(k_y, z)$ in Refs. [147,148].

We focus on the SDOS at the [100] edge shown in Figs. 2(a) (p_x-wave UM-SC) and 3(a) (p_y-wave UM-SC). In Figs. 2(b), 2(c), 3(b), and 3(c), we plot the momentum-resolved SDOS $\rho(E, k_y)$ at $(t_x, t_y) = (t, 0)$ (p_x-wave UM-SC) [Figs. 2(b) and 2(c)], and $(t_x, t_y) = (0, t)$ (p_y-wave UM-SC) [Figs. 3(b) and 3(c)]. The chemical potential is chosen as $\mu = -4t$ [Figs. 2(b) and 2(c)], and $\mu = -2t$ [Figs. 3(b) and 3(c)]. Because noncollinear spin structure exhibits in the zx plane for both t_x and J shown in Fig. 2(a), at $\mu = -4t$, both nodal points and zero-energy flat bands appear [Fig. 3(b)] [149,150]. While in Fig. 3(a), noncollinear spin structure emerges in the yz plane for both t_y and J. Then the noncollinear spin structure aligns along the [100] edge, and as a result, we only obtain the nodal structure [Fig. 3(b)]. At $\mu = -2t$, for the p_x-wave UM-SC [$(t_x, t_y) = (t, 0)$], zero-energy flat bands partly appear by connecting two nodal points shown in Fig. 2(c) [14], while for the p_y-wave UM-SC [$(t_x, t_y) = (0, t)$], only nodal structure appears [Fig. 3(c)]. We demonstrate the bulk energy gap structure (quasiparticle energy dispersions), and we confirm that the energy gap is closing in PUM-SCs and the nodal structure emerges for $J > \Delta$, in Appendix A. Indeed, these SDOS structures are effectively similar to the spin-triplet p_x [Fig. 2(b)] and p_y-wave superconductivity [Fig. 3(b)]. It indicates that the p-wave superconductivity can be realized by PUM, even though we assume the spin-singlet s-wave pairing, and it is characterized by the spin-dependent hopping t_x and t_y. As clarified in Ref. [123], we also obtain the zero-energy flat bands by using the distinct PUM model [54]. We confirm the realization of zero-energy flat bands independent of the chemical potential μ. We note that these zero-energy flat bands are topologically protected by winding numbers [123]. These nodal structures protected by a topological invariant in bulk SCs host the zero-energy flat bands unless the energy gap closes by changing the parameters [15]. Thus, in our study, zero-energy flat bands caused by spin-triplet p-wave superconductivity can be realized within the parameter range.

After the integral for k_y, we obtain the SDOS and bulk DOS $D(E)$ normalized by the normal state SDOS and bulk at zero energy D_{N} at Figs. 2(d) and 2(e) $(t_x, t_y) = (t, 0)$ (p_x-wave UM-SC), and Figs. 3(d) and 3(e) $(t_x, t_y) = (0, t)$ (p_y-wave UM-SC). In the bulk, even though we only assume the spin-singlet s-wave pair potential, we obtain the V-shaped DOS for each case [black dotted lines in Figs. 2(d), 2(e), 3(d), and 3(e)]. This line shape originates from the nodal structure in the bulk (see also Appendix A). For the p_x-wave UM-SC [$(t_x, t_y) = (t, 0)$], at $\mu = -4t$, in the presence of the zero-energy flat bands shown in Fig. 2(b), the zero-energy peak of SDOS is obtained [Fig. 2(d)] [149,150]. At $\mu = -2t$, three peaks of SDOS appear at $E = 0$ and $E \sim \pm 0.3\Delta$, as shown in Fig. 2(e). We note that the peak at $E \sim \pm 0.3\Delta$ originates from the flat bands of the SDOS at $E \sim \pm 0.3\Delta$ in Fig. 2(d). On the other hand, for the p_y-wave UM-SC [$(t_x, t_y) = (0, t)$], because zero-energy flat bands do not exhibit at $\mu = -4t, -2t$ [Figs. 3(b) and 3(c)], the V-shaped SDOS appears [Figs. 3(d)

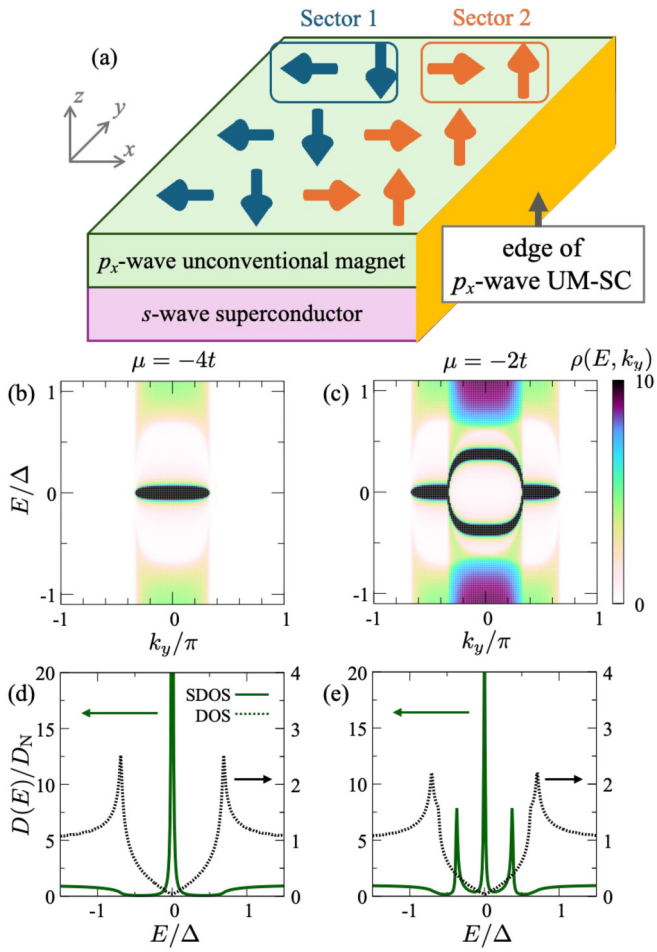


FIG. 2. (a) Schematic illustration of PUM/s-wave SC hybrid systems (p_x-wave UM-SCs) at $t_x \neq 0$ and $t_y = 0$. We also show the two sectors in the effective Hamiltonian of Eq. (1). (b), (c) At the [100] edge, momentum-resolved surface density of states (SDOS) $\rho(E, k_y)$ at (b) $\mu = -4t$ and (c) $\mu = -2t$. (d), (e) SDOS (green solid) and bulk DOS (black dotted lines) normalized by D_N with the normal state SDOS and bulk DOS at zero energy for (d) $\mu = -4t$ and (e) $\mu = -2t$. Parameters: $(t_x, t_y) = (t, 0)$, $J = t$, $\Delta = 0.01t$, and $\delta = 0.01\Delta$.

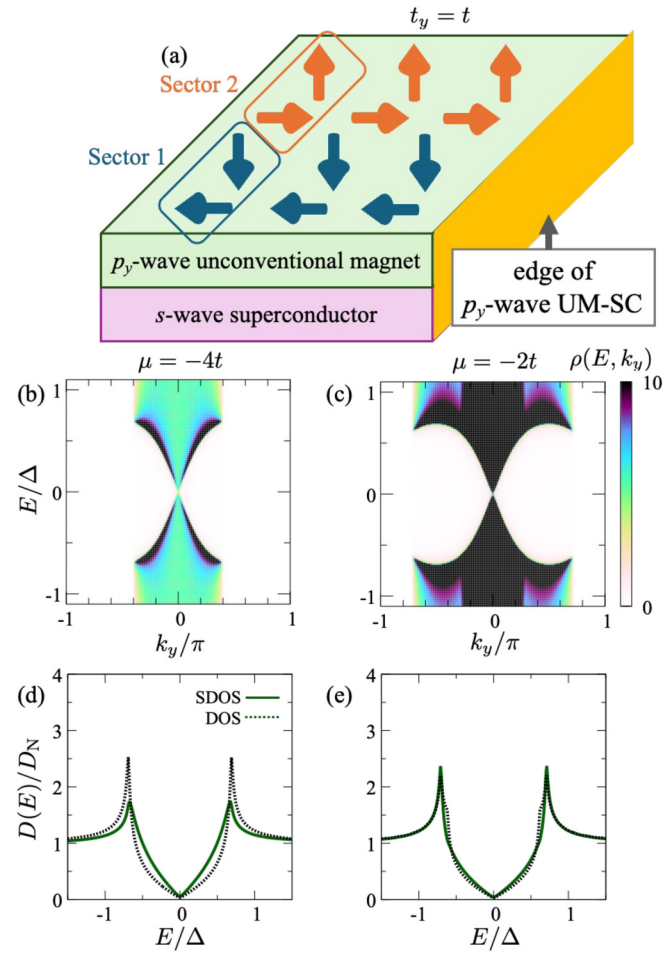


FIG. 3. (a) Schematic illustration of PUM/s-wave SC hybrid systems (p_y-wave UM-SCs) at $t_x = 0$ and $t_y \neq 0$. We also show the two sectors in the effective Hamiltonian of Eq. (1). (b), (c) At the [100] edge, momentum-resolved SDOS $\rho(E, k_y)$ at (b) $\mu = -4t$ and (c) $\mu = -2t$. (d), (e) SDOS (green solid) and bulk DOS (black dotted lines) normalized by D_N with the normal state SDOS and bulk at zero energy for (d) $\mu = -4t$ and (e) $\mu = -2t$. Parameters: $(t_x, t_y) = (0, t)$, $J = t$, $\Delta = 0.01t$, and $\delta = 0.01\Delta$.

and 3(e)]. We note that this line shape originates from the nodal structure at $k_y = 0$ [Figs. 3(b) and 3(c)]. Hence, zero-energy flat bands can be realized in PUM-SCs as the p-wave superconductivity. These zero-energy flat bands can also be interpreted as topologically protected zero modes [8–11].

IV. PAIR AMPLITUDE CONFIGURATIONS AT THE [100] EDGE

Since it is known that odd-frequency pairings emerge in zero-energy flat bands [7,151–153], we here analyze the anomalous electron-hole Green's functions, that is, the pair amplitude, at the [100] edge of PUM-SCs. Pair amplitude $\hat{F}^{\sigma,\sigma'}_{j_x,j'_x}(k_y, i\omega_n)$ with the spin $\sigma, \sigma' = \uparrow, \downarrow$, the site indices along the x direction (j_x, j'_x), and the fermionic Matsubara frequency $\omega_n = (2n+1)\pi k_B T$ for the temperature T at the [100] edge is obtained by the semi-infinite Green's function $(j_x = j'_x = 0)$ with

$$\tilde{G}(k_y, i\omega_n) = \begin{pmatrix} \hat{G}(k_y, i\omega_n) & \hat{F}(k_y, i\omega_n) \\ \bar{F}(k_y, i\omega_n) & \bar{F}(k_y, i\omega_n) \end{pmatrix}, \tag{8}$$

and the anomalous Green's part:

$$\hat{F}(k_y, i\omega_n) = \begin{pmatrix} F^{\uparrow\uparrow}(k_y, i\omega_n) & F^{\uparrow\downarrow}(k_y, i\omega_n) \\ F^{\downarrow\uparrow}(k_y, i\omega_n) & F^{\downarrow\downarrow}(k_y, i\omega_n) \end{pmatrix}. \tag{9}$$

In this study, pair amplitude is classified as even-frequency spin-singlet even parity (ESE), even-frequency spin-triplet odd parity (ETO), odd-frequency spin-singlet odd parity (OSO) [154,155], and odd-frequency spin-triplet even parity (OTE) [155–158]. Then we can calculate the pair amplitude at the edge $(j_x = j'_x = 0)$ as

$$F^{\uparrow\downarrow}_{\mathrm{ESE}}(k_y, i\omega_n) = \tfrac{1}{4}[F^{\uparrow\downarrow}(k_y, i\omega_n) - F^{\downarrow\uparrow}(k_y, i\omega_n) + F^{\uparrow\downarrow}(k_y, -i\omega_n) - F^{\downarrow\uparrow}(k_y, -i\omega_n)], \tag{10}$$

for ESE,

$$F^{\uparrow\downarrow}_{\rm ETO}(k_y, i\omega_n) = \tfrac{1}{4}[F^{\uparrow\downarrow}(k_y, i\omega_n) + F^{\downarrow\uparrow}(k_y, i\omega_n) + F^{\uparrow\downarrow}(k_y, -i\omega_n) + F^{\downarrow\uparrow}(k_y, -i\omega_n)], \quad (11)$$

$$F^{\uparrow\uparrow}_{\rm ETO}(k_y, i\omega_n) = \tfrac{1}{2}[F^{\uparrow\uparrow}(k_y, i\omega_n) + F^{\uparrow\uparrow}(k_y, -i\omega_n)], \quad (12)$$

$$F^{\downarrow\downarrow}_{\rm ETO}(k_y, i\omega_n) = \tfrac{1}{2}[F^{\downarrow\downarrow}(k_y, i\omega_n) + F^{\downarrow\downarrow}(k_y, -i\omega_n)], \quad (13)$$

for ETO,

$$F^{\uparrow\downarrow}_{\rm OSO}(k_y, i\omega_n) = \tfrac{1}{4}[F^{\uparrow\downarrow}(k_y, i\omega_n) - F^{\downarrow\uparrow}(k_y, i\omega_n) - F^{\uparrow\downarrow}(k_y, -i\omega_n) + F^{\downarrow\uparrow}(k_y, -i\omega_n)], \quad (14)$$

for OSO, and

$$F^{\uparrow\downarrow}_{\rm OTE}(k_y, i\omega_n) = \tfrac{1}{4}[F^{\uparrow\downarrow}(k_y, i\omega_n) + F^{\downarrow\uparrow}(k_y, i\omega_n) - F^{\uparrow\downarrow}(k_y, -i\omega_n) - F^{\downarrow\uparrow}(k_y, -i\omega_n)], \quad (15)$$

$$F^{\uparrow\uparrow}_{\rm OTE}(k_y, i\omega_n) = \tfrac{1}{2}[F^{\uparrow\uparrow}(k_y, i\omega_n) - F^{\uparrow\uparrow}(k_y, -i\omega_n)], \quad (16)$$

$$F^{\downarrow\downarrow}_{\rm OTE}(k_y, i\omega_n) = \tfrac{1}{2}[F^{\downarrow\downarrow}(k_y, i\omega_n) - F^{\downarrow\downarrow}(k_y, -i\omega_n)], \quad (17)$$

for OTE pairings.

In the bulk, we can obtain the analytical solutions of the pair amplitude (see also Appendix B). When we select $t_x \neq 0$ and $t_y = 0$, ETO pairing is given by

$$F^{\uparrow\uparrow}_{\rm ETO} = F^{\downarrow\downarrow}_{\rm ETO} = \frac{2\Delta\eta J t_x \sin k_x}{D_x}, \quad (18)$$

and OTE pairing is given by

$$F^{\uparrow\uparrow}_{\rm OTE} = F^{\downarrow\downarrow}_{\rm OTE} = \frac{2i\Delta\eta J\omega_n}{D_x}, \quad (19)$$

with $\eta = \pm 1$ and

$$D_x = t_x^4 \sin^4 k_x + \Delta^4 + \varepsilon^4(\boldsymbol{k}) + J^2 - 2\varepsilon^2(\boldsymbol{k})J^2 + 2\varepsilon^2(\boldsymbol{k})\omega_n^2 + 2J^2\omega_n^2 + \omega_n^4 + 2\Delta^2\left[\varepsilon^2(\boldsymbol{k}) - J^2 + \omega_n^2\right] + 2t_x^2 \sin^2 k_x\left[\Delta^2 - \varepsilon^2(\boldsymbol{k}) + J^2 + \omega_n^2\right]. \quad (20)$$

We obtain these equations as worked in Appendix B. ETO pairing is induced by both nonzero $t_{x,y}$ and J; however, OTE pairing can be exhibited with nonzero J, and it is independent of $t_{x,y}$.

While at the edge, we need to calculate the semi-infinite Green's function for $\omega_n = \pi k_{\rm B} T$ to evaluate the pair amplitude. Calculating the pair amplitude for $\omega_n = \pi k_{\rm B} T$, we assume that the superconducting energy gap amplitude has the temperature T dependence that obeys the BCS theory:

$$\Delta(T) = \Delta_0 \tanh\left[1.74\sqrt{\frac{T_{\rm c} - T}{T}}\right], \quad (21)$$

with the gap amplitude at zero temperature $\Delta_0 = 1.76 T_{\rm c}$ and the critical temperature $T_{\rm c} = 0.01t$. In this section, we choose the temperature as $T = 0.025 T_{\rm c}$.

We plot the absolute value of the pair amplitude for ESE and OTE pairings at $(t_x, t_y) = (t, 0)$ (p_x-wave UM) in Fig. 4. Then we clarify the pair amplitude by the lowest Matsubara frequency $\omega_n = \pi k_{\rm B} T$. In this case, ETO and OSO components vanish at the [100] edge owing to the nonlocal pairings along the x direction. As shown in Appendix B, ETO pairing with equal spins is dominant in the bulk. At the [100] edge, at $\mu = -4t$ in Figs. 4(a) and 4(c), the OTE pairing $|F^{\uparrow\uparrow,\downarrow\downarrow}_{\rm OTE}(k_y, i\omega_n)|$ is around 800 times larger than ESE $|F^{\uparrow\downarrow}_{\rm ESE}(k_y, i\omega_n)|$. Then the OTE component is enhanced in the presence of zero-energy flat bands [Fig. 2(b)]. At $\mu = -2t$, ESE pairing becomes large [Fig. 4(b)] as compared with at $\mu = -4t$ [Fig. 4(a)], and nonzero values appear in the absence of zero-energy flat bands [Fig. 2(c)], while OTE pairing is also enhanced in the presence of zero-energy flat bands [Fig. 2(c)].

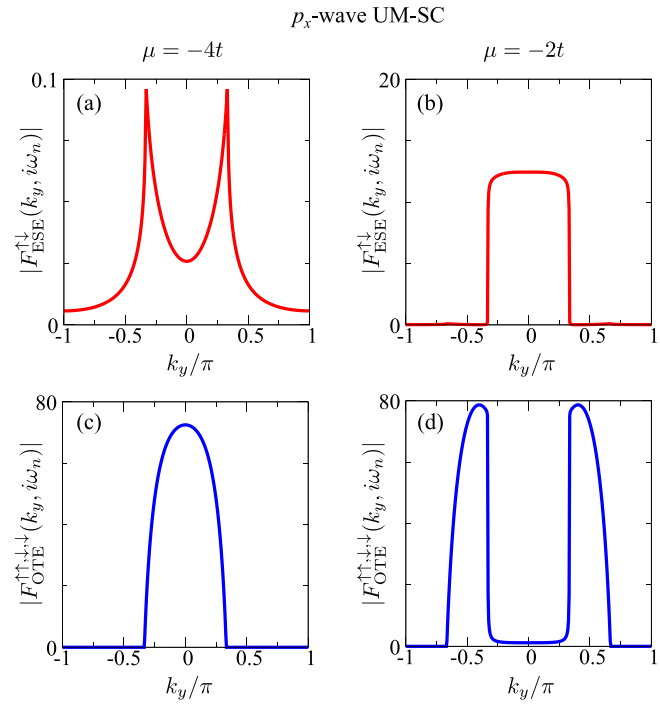


FIG. 4. Absolute value of the pair amplitude for (a), (b) even-frequency spin-singlet even-parity (ESE) and (c), (d) odd-frequency spin-triplet even-parity (OTE) pairings at the [100] edge of PUM-SCs at $t_x = t$. We plot the pair amplitude at the lowest Matsubara frequency $\omega_n = \pi k_{\rm B} T$. The functions of $|F^{\uparrow\uparrow}_{\rm OTE}|$ and $|F^{\downarrow\downarrow}_{\rm OTE}|$ for k_y are the same. Parameters: $(t_x, t_y) = (t, 0)$, $J = t$, $T_{\rm c} = 0.01t$, and $T = 0.025 T_{\rm c}$.

At $(t_x, t_y) = (0, t)$ (p_y-wave UM) in Fig. 5, we also obtain ESE, ETO, and OTE pairings at the [100] edge. Because the ETO pairing is odd for k_y in the bulk, as we worked in Appendix B, its component becomes nonzero at the edge [Figs. 5(c) and 5(d)]. As well as the p_x-wave UM-SC, ETO pairing is also dominant in the bulk (see also Appendix B). As compared with $(t_x, t_y) = (t, 0)$ (p_x-wave UM-SC) in Fig. 4, ESE and ETO pairings are dominant. Because we do not obtain zero-energy flat bands at $(t_x, t_y) = (0, t)$ (p_y-wave UM-SC), OTE pairing is smaller than other pair amplitudes in Fig. 5. These behaviors are consistent with the fact that the OTE state is enhanced at the edge in the presence of zero-energy flat bands. However, ESE pairing does not vanish, even though p-wave superconductivity emerges in PUM-SCs.

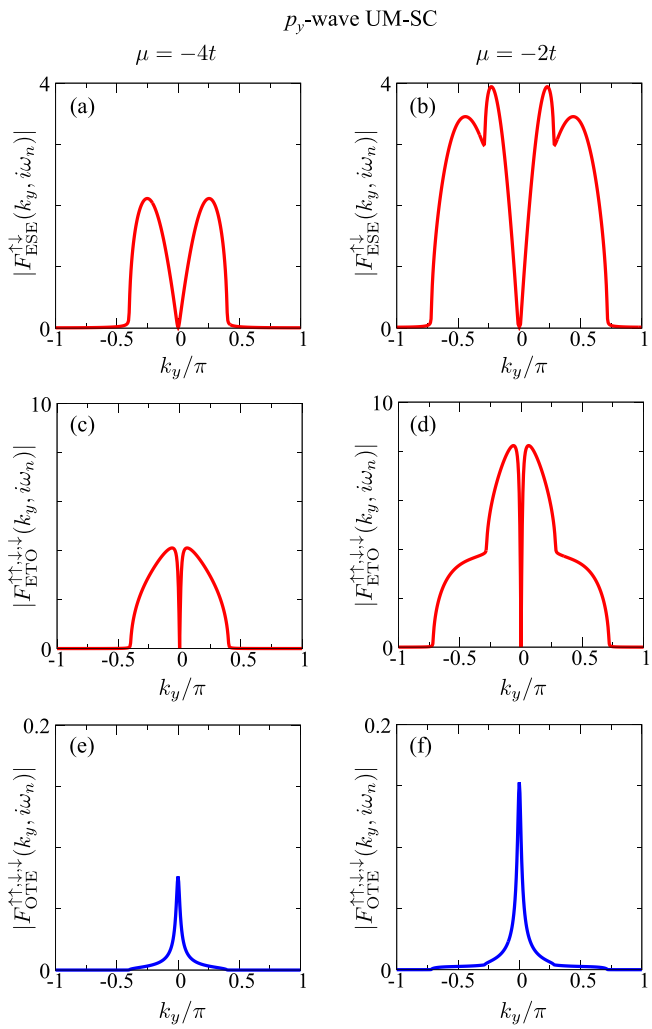


FIG. 5. Absolute value of the pair amplitude for (a), (b) even-frequency spin-singlet even-parity (ESE), (c), (d) even-frequency spin-triplet odd-parity (ETO), and (e), (f) odd-frequency spin-triplet even-parity (OTE) pairings at the [100] edge of PUM-SCs at $t_y = t$. We plot the pair amplitude at the lowest Matsubara frequency $\omega_n = \pi k_{\rm B} T$. The function of $|F^{\uparrow\uparrow}_{\rm ETO}|$ and $|F^{\downarrow\downarrow}_{\rm ETO}|$ for k_y are the same. Parameters: $(t_x, t_y) = (0, t)$, $J = t$, $T_{\rm c} = 0.01t$, and $T = 0.025T_{\rm c}$.

Indeed, ETO pairing with equal spins is dominant in the bulk, and OTE pairing that is enhanced in the presence of zero-energy flat bands can also exist at the edge of PUM-SCs. Then, the magnitude of the ESE pairing at the [100] edge is suppressed in the presence of zero-energy flat bands.

V. JOSEPHSON CURRENT IN PUM-SCS IN THE HIGH-TRANSPARENCY LIMIT

Next, we demonstrate the Josephson current in Josephson junctions with PUM-SCs. In the present study, we assume the periodic boundary condition along the y direction and semi-infinite SCs on both sides of the junctions. Then we also consider two layers in the normal metal of the junction (see also Appendix C). In the tight-binding model, the Josephson current is calculated by [80,159–162]

$$I(\varphi) = \frac{iek_{\rm B}T}{\hbar} \int dk_y \sum_{\omega_n} {\rm Tr}'[\tilde{t}_{\rm N}^{\dagger} \tilde{G}_{0,1}(k_y, i\omega_n) - \tilde{t}_{\rm N} \tilde{G}_{1,0}(k_y, i\omega_n)], \tag{22}$$

where T is the temperature, $\tilde{t}_{\rm N}$ is the nearest-neighbor hopping term in the normal metal, and $\tilde{G}_{0,1}(k_y, i\omega_n)$ and $\tilde{G}_{1,0}(k_y, i\omega_n)$ are the nonlocal Green's functions (see also Appendix C). We summarize the formulation of the Josephson current in Appendix C.

In this study, we have revealed that the current phase relation is described by the odd function of the Fourier series [163]:

$$I(\varphi) = \sum_m I_m \sin(m\varphi), \tag{23}$$

with the phase difference φ. We hereby focus on the high-transparency limit, with the higher harmonics components I_m [164]. Then we choose the transparency amplitude as $t_{\rm int} = 1.0$ (see also Appendix C).

A. PUM-SC/spin-singlet s-wave SC Josephson junctions

First of all, we study the Josephson current in PUM-SC/spin-singlet s-wave SC Josephson junctions shown in Fig. 6(a). In the normal metal, the Hamiltonian is given by

$$\hat{H}_{\rm N}(\boldsymbol{k}) = [-\mu_{\rm N} - 2t\cos k_x - 2t\cos k_y]\hat{s}_0, \tag{24}$$

with the chemical potential in the normal metal $\mu_{\rm N} = -3.5t$. In spin-singlet s-wave SCs, we assume the following Bogoliubov–de Gennes Hamiltonian:

$$\hat{H}^s_{\rm BdG} = \begin{pmatrix} \hat{H}_s(\boldsymbol{k}) & \hat{\Delta}_s \\ \hat{\Delta}_s^{\dagger} & \hat{H}_s(\boldsymbol{k}) \end{pmatrix}, \tag{25}$$

$$\hat{H}_s(\boldsymbol{k}) = [-\mu_s - 2t\cos k_x - 2t\cos k_y]\hat{s}_0, \tag{26}$$

$$\hat{\Delta}_s = \Delta_s(T) i\hat{s}_2, \tag{27}$$

$$\Delta_s(T) = \bar{\Delta}_s \tanh\left[1.74\sqrt{\frac{T_{\rm c} - T}{T}}\right], \tag{28}$$

with the chemical potential in spin-singlet s-wave SCs $\mu_s = -1.5t$ and the superconducting energy gap amplitude $\bar{\Delta}_s$. Since the materials are different, we choose the distinct values of the chemical potentials in the spin-singlet s-wave SC μ_s and the normal metal $\mu_{\rm N}$. Although the magnitude of the pair potential in PUM-SC $\bar{\Delta}_p$,

$$\Delta_p(T) = \bar{\Delta}_p \tanh\left[1.74\sqrt{\frac{T_{\rm c} - T}{T}}\right], \tag{29}$$

with the gap amplitude at zero temperature $\bar{\Delta}_p = p\Delta_0$, is smaller than that in spin-singlet s-wave SCs $\bar{\Delta}_s$ [165], here, we choose $\bar{\Delta}_p = \Delta_0$ $(p = 1)$ and $\bar{\Delta}_s = \Delta_0$ for simplicity. The current phase relations do not change qualitatively even though we set the smaller $\bar{\Delta}_s$ than Δ_0 at high transparency, as shown in Appendix D.

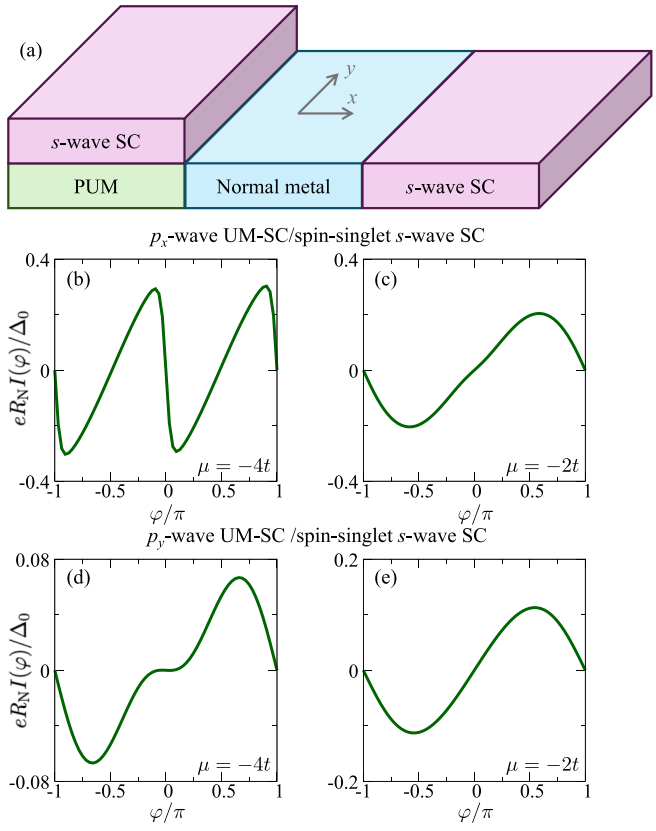


FIG. 6. (a) Schematic image of PUM-SC/spin-singlet s-wave SC Josephson junctions. (b)–(e) Current phase relation in PUM-SC/spin-singlet s-wave SC Josephson junctions at (b), (c) $(t, t_y) = (t, 0)$ and (d), (e) $(t_x, t_y) = (0, t)$. We select the chemical potential as (b), (d) $\mu = -4t$ and (c), (e) $\mu = -2t$. Parameters: $\mu_N = -3.5t$, $\mu_s = -1.5t$, $J = t$, $p = 1$, $T_c = 0.01t$, $T = 0.025T_c$, and $t_{int} = 1$.

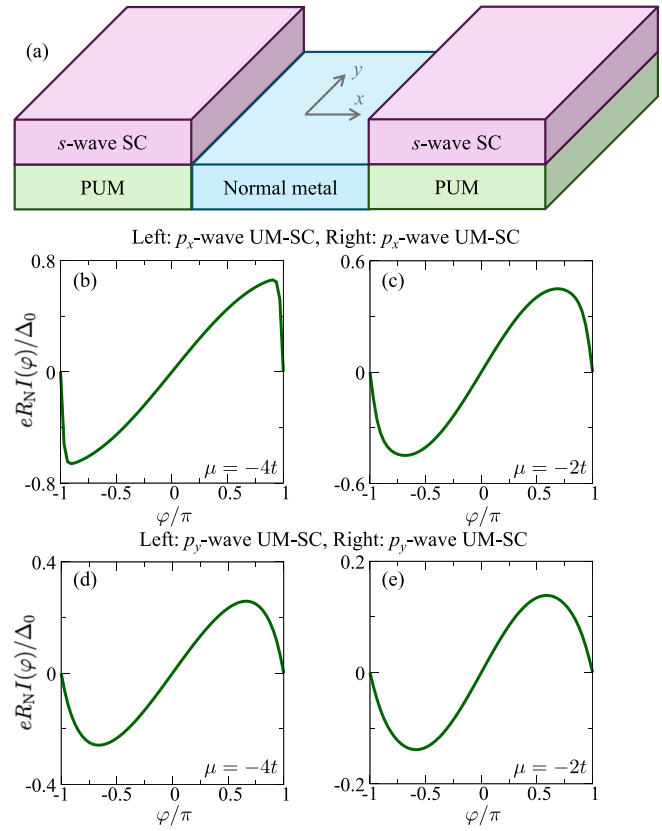


FIG. 7. (a) Schematic image of PUM-SC/PUM-SC Josephson junctions. (b)–(e) Current phase relation in PUM-SC/PUM-SC Josephson junctions at (b), (c) $(t_x^L, t_y^L; t_x^R, t_y^R) = (t, 0; t, 0)$ and (d), (e) $(t_x^L, t_y^L; t_x^R, t_y^R) = (0, t; 0, t)$. We choose the chemical potential as (b), (d) $\mu^L = \mu^R = -4t$ and (c), (e) $\mu^L = \mu^R = -2t$. Parameters: $\mu_N = -3.5t$, $J^L = J^R = t$, $T_c = 0.01t$, $T = 0.025T_c$, and $t_{int} = 1$.

For the p_x-wave UM-SC at $(t_x, t_y) = (t, 0)$, we plot the current phase relation in Figs. 6(b), $\mu = -4t$, and 6(c), $\mu = -2t$. Although the I_2 term is dominant at $\mu = -4t$ [Fig. 6(b)], the I_1 component remains. It originates from the ESE pair amplitude at the [100] edge [Fig. 4(a)], even though we obtain zero-energy flat bands caused by p_x-wave superconductivity at $\mu = -4t$ as shown in Fig. 2(b). Because this ESE pair amplitude on the left side is coupled to the spin-singlet s-wave superconductivity on the right side by the first order, the I_1 term does not disappear in Fig. 6(b). In p_x-wave SC/spin-singlet s-wave SC Josephson junctions, the current phase relation is described by $I_2 \sin(2\varphi)$, and I_1 vanishes [50]. It indicates that PUM-SC/spin-singlet s-wave SC Josephson junctions are not equivalent to p_x-wave SC/s-wave SC ones. As well as at $\mu = -2t$ [Fig. 6(c)], I_1 becomes nonzero and it is dominant as compared with higher $I_{m\geq 2}$. Since the amplitude of the ESE component at $\mu = -2t$ [Fig. 4(b)] is 200 times larger than that at $\mu = -4t$ [Fig. 4(a)], the configuration of I_1 is also enhanced. We note that π junctions [166] do not appear due to the conventional spin-singlet s-wave coupling on both sides of the junctions. Likewise, for the p_y-wave UM-SC case at $(t_x, t_y) = (0, t)$, the I_1 component is also dominant at $\mu = -4t$ [Fig. 6(d)] and $\mu = -2t$ [Fig. 6(e)] owing to the larger ESE pair amplitude [Figs. 5(a) and 5(b)]. It is also noted that the current phase relations in Figs. 6(b) and 6(d) are φ junctions, where the free energy minima of the junctions are located $\pm\varphi$ with degeneracy. Hence, the conventional current phase relation with $I_1 > 0$ mainly emerges in PUM-SC/spin-singlet s-wave Josephson junctions. It indicates that the current phase relation of PUM-SC/spin-singlet s-wave SC Josephson junctions does not coincide with that of p-wave SC/s-wave SC Josephson junctions, even though p-wave superconductivity is realized in PUM-SCs. In Appendix D, we also show the current phase relations when changing the magnitude of the pair potential in PUM-SC at $p = 0.1$, and the qualitative results of the current phase relations do not change.

B. PUM-SC/PUM-SC Josephson junctions

Next, we study the current phase relation in PUM-SC/PUM-SC Josephson junctions [Fig. 7(a)]. Then we introduce the parameters on the left side, $(\mu^L, t_x^L, t_y^L, J^L)$, and the right side, $(\mu^R, t_x^R, t_y^R, J^R)$, respectively. For simplicity, we choose $\mu = \mu^L = \mu^R$, $J^L = J^R = t$, and the same critical temperature T_c and the amplitude of the pair potential $\Delta(T)$ in Eq. (21) in Josephson junctions.

At $(t_x^L, t_y^L; t_x^R, t_y^R) = (t, 0; t, 0)$ (left, p_x-wave UM-SC; right, p_x-wave UM-SC), for $\mu = -4t$, the current

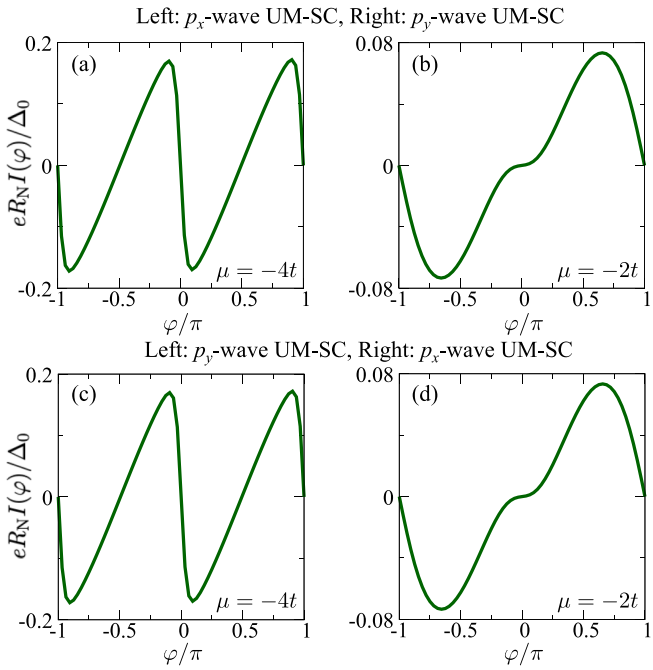


FIG. 8. Current phase relation in PUM-SC/PUM-SC Josephson junctions at (a), (b) $(t_x^{\rm L}, t_y^{\rm L}; t_x^{\rm R}, t_y^{\rm R}) = (t, 0; 0, t)$ and (c), (d) $(t_x^{\rm L}, t_y^{\rm L}; t_x^{\rm R}, t_y^{\rm R}) = (0, t; t, 0)$. We choose the chemical potential as (a), (c) $\mu^{\rm L} = \mu^{\rm R} = -4t$ and (b), (d) $\mu^{\rm L} = \mu^{\rm R} = -2t$. Parameters: $\mu_{\rm N} = -3.5t$, $J = t$, $T_{\rm c} = 0.01t$, $T = 0.025T_{\rm c}$, and $t_{\rm int} = 1$.

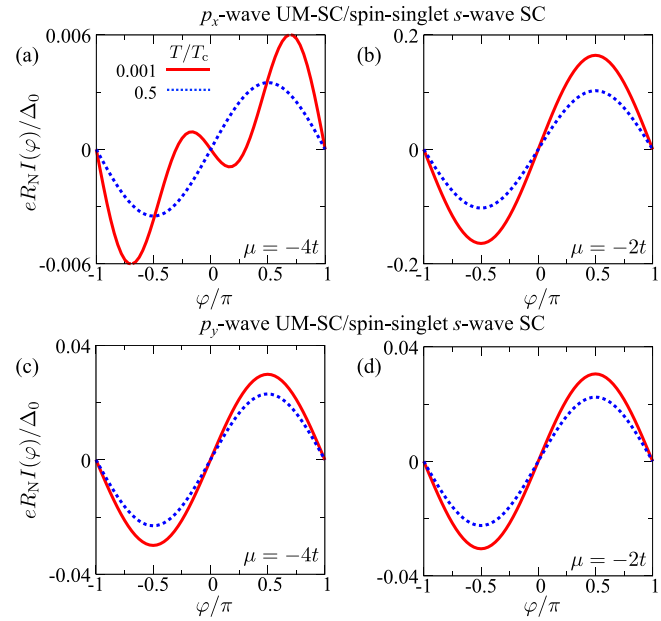


FIG. 9. Current phase relation in PUM-SC/spin-singlet s-wave SC Josephson junctions at (a), (b) $(t_x, t_y) = (t, 0)$ and (c), (d) $(t_x, t_y) = (0, t)$. We select the chemical potential as (a), (c) $\mu = -4t$ and (b), (d) $\mu = -2t$. Red-solid and blue-dotted lines correspond to the temperature $T = 0.001T_{\rm c}$ and $0.5T_{\rm c}$, respectively. Parameters: $\mu_{\rm N} = -3.5t$, $\mu_s = -1.5t$, $J = t$, $p = 1$, $T_{\rm c} = 0.01t$, and $t_{\rm int} = 0.1$.

phase relation becomes maximum around $\varphi = \pm\pi$ [Fig. 7(b)]. Then, the skewness of the current phase relation becomes remarkable in the presence of zero-energy flat bands. This behavior is similar to that known in p_x-wave SC/p_x-wave SC Josephson junctions [51–53]. However, for $\mu = -2t$ shown in Fig. 7(c), the skewness effect in the current phase relation is suppressed. Although the effective transparency for $\mu = -2t$ is distinct from that for $\mu = -4t$, this behavior is caused by the smaller regime of zero-energy flat bands formed in the momentum space [Fig. 2(c)] compared with Fig. 2(b). In Fig. 7(d) for $\mu = -4t$ and Fig. 7(e) for $\mu = -2t$, at $(t_x^{\rm L}, t_y^{\rm L}; t_x^{\rm R}, t_y^{\rm R}) = (0, t; 0, t)$ (left, p_y-wave UM-SC; right, p_y-wave UM-SC), we obtain the I_1-dominant current phase relations. We also calculate the current phase relation at $(t_x^{\rm L}, t_y^{\rm L}; t_x^{\rm R}, t_y^{\rm R}) = (t, 0; 0, t)$ (left, p_x-wave UM-SC; right, p_y-wave UM-SC) and $(t_x^{\rm L}, t_y^{\rm L}; t_x^{\rm R}, t_y^{\rm R}) = (0, t; t, 0)$ (left, p_y-wave UM-SC; right, p_x-wave UM-SC) shown in Fig. 8. Because induced spin-triplet pairings with different mirror symmetries in the zx plane are coupled within the second order, the current phase relation does not change by the exchange of the left and right sides (Fig. 8). For $\mu = -4t$, I_2-dominant behavior is obtained, and then I_1 is nonzero [Figs. 8(a) and 8(c)]. In Figs. 8(b) and 8(d), for $\mu = -2t$, I_1 is comparable with I_2. These behaviors correspond to the φ junctions [36,39]. Indeed, the coupling of the spin-triplet p-wave pair amplitude on both sides of the junctions contributes to the current phase relation; however, spin-singlet pairings also play a role in the current phase relation of PUM-SC/PUM-SC Josephson junctions.

VI. TEMPERATURE DEPENDENCE OF THE MAXIMUM JOSEPHSON CURRENT IN PUM-SCS IN THE LOW-TRANSPARENCY LIMIT

In this section, we calculate not only the current phase relation but also the temperature dependence of the maximum Josephson current in PUM-SCs. Then we focus on the low transparency, and we select the transparency amplitude as $t_{\rm int} = 0.1$ (see also in Appendix C).

In PUM-SC/spin-singlet s-wave Josephson junctions, we plot the current phase relations at $T = 0.001T_{\rm c}$ (red-solid) and $T = 0.5T_{\rm c}$ (blue-dotted lines) as shown in Fig. 9. Then, we set the temperature dependence of the magnitude of the pair potential as Eq. (29) at $p = 1$ in PUM-SC and Eq. (28) in spin-singlet s-wave SCs. At $T = 0.001T_{\rm c}$, for $(t_x, t_y, \mu) = (t, 0, -4t)$ (p_x-wave UM-SC) [Fig. 9(a)], the φ junction appears owing to the strong resonance of zero-energy flat bands in p_x-wave UM-SCs [37,39]. In Appendix D, for $(t_x, t_y, \mu) = (t, 0, -4t)$, we confirm the current phase relations at $p = 0.1$. The nonsinusoidal feature disappears at $T = 0.001T_{\rm c}$. Due to the enhancement of higher harmonics in the current phase relation $I_{m\geqslant 2}$ at low temperature, the maximum Josephson current $I_{\rm c}$ is also enhanced, although $I_{\rm c}$ is once saturated [Fig. 10(a)]. Because the region of zero-energy flat bands in the momentum space for $\mu = -2t$ is smaller than that for $\mu = -4t$ [Figs. 2(b) and 2(c)], the $I_1 \sin\varphi$ dependence is mainly dominant for $(t_x, t_y, \mu) = (t, 0, -2t)$ (p_x-wave UM-SC) [Fig. 9(b)], while, for $(t_x, t_y, \mu) = (0, t, -4t)$ [Fig. 9(c)] and $(t_x, t_y, \mu) = (0, t, -2t)$ (p_y-wave UM-SC) [Fig. 9(d)], we obtain $I_1 \sin\varphi$ behaviors, and it is known that the current phase relation in conventional s-wave SC junctions is described by

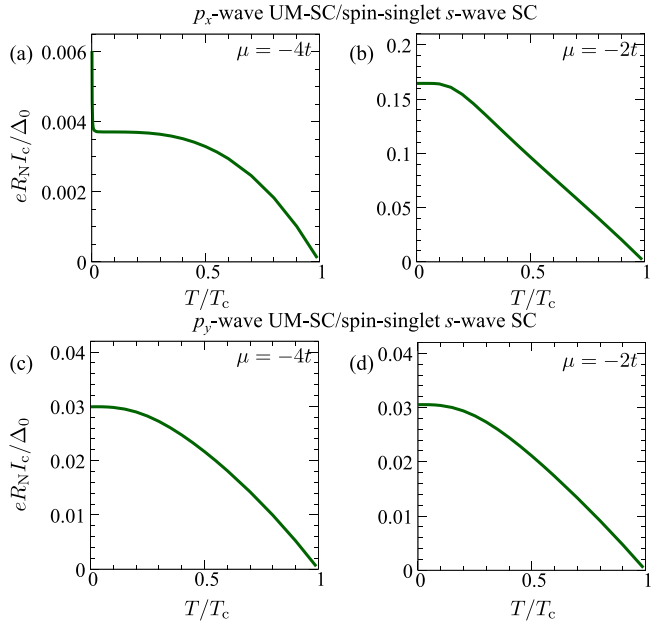


FIG. 10. Temperature dependence of the maximum Josephson current I_c in PUM-SC/spin-singlet s-wave SC Josephson junctions at (a) $(t_x, t_y, \mu) = (t, 0, -4t)$, (b) $(t_x, t_y, \mu) = (t, 0, -2t)$, (c) $(t_x, t_y, \mu) = (0, t, -4t)$, and (d) $(t_x, t_y, \mu) = (0, t, -2t)$. Parameters: $\mu_N = -3.5t$, $\mu_s = -1.5t$, $J = t$, $T_c = 0.01t$, $p = 1$, $\Delta_0 = 1.76T_c$, and $t_{int} = 0.1$.

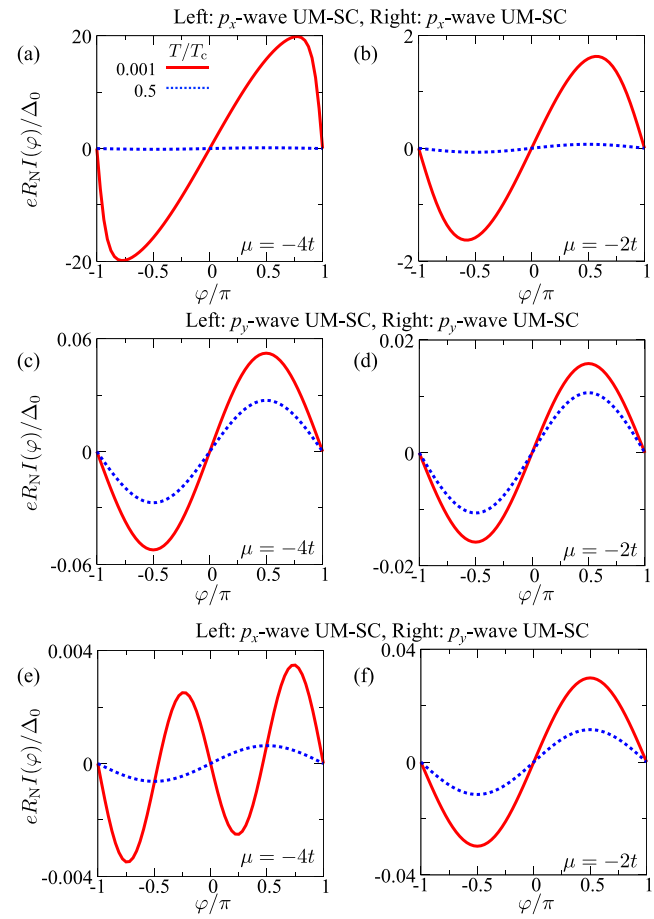


FIG. 11. Current phase relation in PUM-SC/PUM-SC Josephson junctions at (a), (b) $(t_x^L, t_y^L; t_x^R, t_y^R) = (t, 0; t, 0)$, (c), (d) $(t_x^L, t_y^L; t_x^R, t_y^R) = (0, t; 0, t)$, and (e), (f) $(t_x^L, t_y^L; t_x^R, t_y^R) = (t, 0; 0, t)$. We choose the chemical potential as (a), (c), (e) $\mu = \mu^L = \mu^R = -4t$ and (b), (d), (f) $\mu = \mu^L = \mu^R = -2t$. Red-solid and blue-dotted lines correspond to the temperature $T = 0.001T_c$ and $0.5T_c$, respectively. Parameters: $\mu_N = -3.5t$, $J^L = J^R = t$, $T_c = 0.01t$, and $t_{int} = 0.1$.

$I(\varphi) = I_1 \sin\varphi$ (Ambegaokar-Baratoff behavior) in the low-transparency limit [42], as well as at $T = 0.50T_c$. The current phase relations do not change qualitatively at $(t_x, t_y, \mu) = (t, 0, -2t)$, $(0, t, -4t)$, and $(t_x, t_y, \mu) = (0, t, -2t)$; see Appendix D. The maximum Josephson current I_c for $(t_x, t_y, \mu) = (t, 0, -2t)$ (p_x-wave UM-SC) [Fig. 10(b)], $(t_x, t_y, \mu) = (0, t, -4t)$ [Fig. 10(c)], and $(t_x, t_y, \mu) = (0, t, -2t)$ (p_y-wave UM-SC) [Fig. 10(d)] is saturated at low temperature, and this behavior is independent of both the chemical potential $\mu = -4t, -2t$ and the spin-dependent hopping terms $t_{x,y}$. As we showed in Fig. 9, the I_1 component does not vanish owing to the coupling of even-frequency spin-singlet even-parity pairings on both sides of the junctions. In the case when the current phase relation becomes sinusoidal behavior that is obtained by Ambegaokar and Baratoff [42], the maximum Josephson current is saturated at low temperature. As a result, in PUM-SC/spin-singlet s-wave junctions, we do not obtain the same temperature dependence as in spin-triplet p-wave SC/spin-singlet s-wave SC junctions without PUM. Since the current phase relations depend on $\bar{\Delta}_p$, the temperature dependence is influenced by the choice of $\bar{\Delta}_p$.

Next, we discuss the current phase relation and temperature dependence of Josephson current in PUM-SC/PUM-SC junctions. In the current phase relation shown in Fig. 11, at $T = 0.5T_c$ (blue-dotted line), we obtain $I_1 \sin\varphi$ behavior in all cases. Then, we select the temperature dependence of the magnitude of the pair potential as Eq. (21). At $T = 0.001T_c$ (red-solid line), for $(t_x^L, t_y^L; t_x^R, t_y^R) = (t, 0; t, 0)$ (left, p_x-wave UM-SC; right, p_x-wave UM-SC) with the chemical potential $\mu = -4t, -2t$, the current phase relation has a skewness [Figs. 11(a) and 11(b)]. We note that the skewness at $\mu = -2t$ is not remarkable due to the smaller region of zero-energy flat bands in the momentum space as compared with that for $\mu = -4t$ [Figs. 2(b) and 2(c)]. The maximum Josephson current I_c, in Figs. 12(a) and 12(b), at $(t_x^L, t_y^L; t_x^R, t_y^R) = (t, 0; t, 0)$ (left, p_x-wave UM-SC; right, p_x-wave UM-SC), is enhanced at low temperature for $\mu = -4t, -2t$. This behavior originates from the resonance of zero-energy flat bands [Figs. 2(b) and 2(c)] on both sides of the junctions, similar to the case in d-wave SC junctions [37,39]. For $(t_x^L, t_y^L; t_x^R, t_y^R) = (t, 0; 0, t)$ (left, p_x-wave UM-SC; right, p_y-wave UM-SC) with the chemical potential $\mu = -4t$, the φ junction emerges [Fig. 11(e)], as we showed in p_x-wave UM-SC/p_y-wave UM-SC junctions for $\mu = -4t$ at the high-transparency limit [Fig. 8(a)]. Then, once I_c is saturated, it is enhanced, with the decrease of the temperature T [Fig. 12(e)]. This enhancement is caused by the resonance of zero-energy flat bands in p_x-wave UM-SCs of the left side [37,39]. In the other cases, at $(t_x^L, t_y^L; t_x^R, t_y^R) = (0, t; 0, t)$ (left, p_y-wave UM-SC; right, p_y-wave UM-SC) for $\mu = -4t, -2t$ and at $(t_x^L, t_y^L; t_x^R, t_y^R) =$

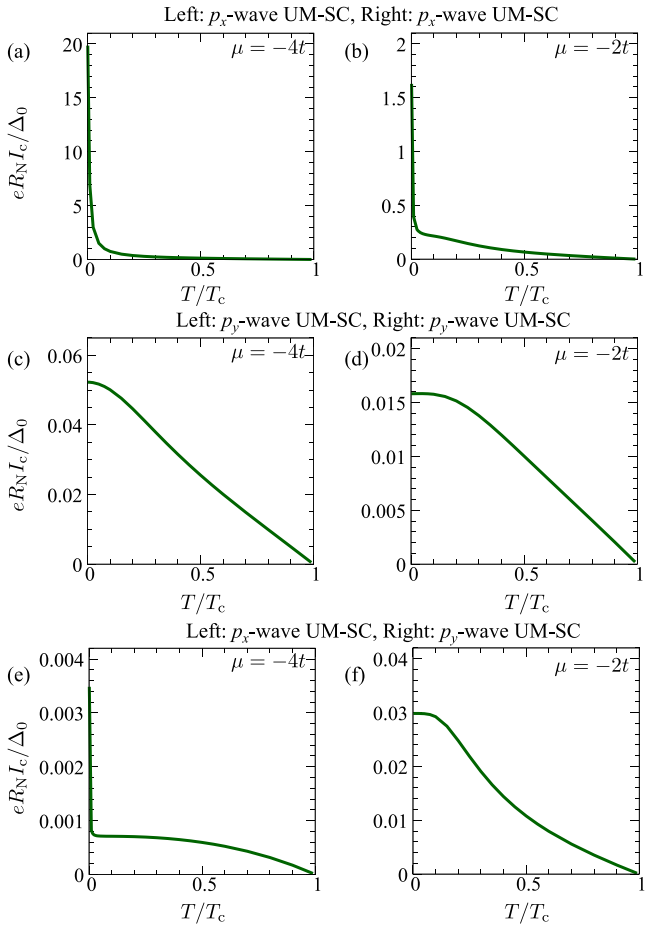


FIG. 12. Temperature dependence of the maximum Josephson current I_c in PUM-SC/PUM-SC Josephson junctions at (a), (b) $(t_x^L, t_y^L; t_x^R, t_y^R) = (t, 0; t, 0)$, (c), (d) $(t_x^L, t_y^L; t_x^R, t_y^R) = (0, t; 0, t)$, and (e), (f) $(t_x^L, t_y^L; t_x^R, t_y^R) = (t, 0; 0, t)$. We choose the chemical potential as (a), (c), (e) $\mu = \mu^L = \mu^R = -4t$ and (b), (d), (f) $\mu = \mu^L = \mu^R = -2t$. Parameters: $\mu_N = -3.5t$, $J = t$, $T_c = 0.01t$, $\Delta_0 = 1.76T_c$, and $t_{int} = 0.1$.

$(t, 0; 0, t)$ (left, p_x-wave UM-SC; right, p_y-wave UM-SC) for $\mu = -2t$, we obtain $I_1 \sin\varphi$ dependence in [Figs. 11(c), 11(d), and 11(f)]. At $(t_x^L, t_y^L; t_x^R, t_y^R) = (0, t; 0, t)$ (left, p_y-wave UM-SC; right, p_y-wave UM-SC) for $\mu = -4t, -2t$, I_c is saturated at low temperature [Figs. 12(c) and 12(d)], in the absence of zero-energy flat bands [Figs. 3(b) and 3(c)]. Likewise, at $(t_x^L, t_y^L; t_x^R, t_y^R) = (t, 0; 0, t)$ (left, p_x-wave UM-SC; right, p_y-wave UM-SC) for $\mu = -2t$, the behavior of I_c changes [Fig. 12(f)], as compared with Fig. 12(e). Since the region of zero-energy flat bands in the momentum space at $\mu = -2t$ is narrower than that at $\mu = -4t$, the enhancement of I_c does not occur in Fig. 12(f). Hence, the spin-triplet p-wave pair amplitude in PUM-SCs can contribute to the current phase relation of the Josephson current with temperature, as well as the existence of zero-energy flat bands.

VII. SUMMARY AND CONCLUSION

We have studied SDOS at the [100] edge in PUM-SCs. We have shown that zero-energy flat bands can exist owing to the noncollinear spin structure in the zx plane, and then p-wave magnetic order can generate p-wave superconductivity. We note that noncollinear spin structure in the xy plane can also lead to zero-energy flat bands at the [100] edge. Similar behavior has already been theoretically proposed in a one-dimensional spin helix/s-wave SC hybrid system [23] and magnetic chain [26]. Indeed, our results are qualitatively consistent with these previous works [26,167–170].

We have also investigated the Josephson current in superconducting junctions with PUM-SCs. In the high-transparency limit, in PUM-SC/spin-singlet s-wave SC Josephson junctions, even though p-wave superconductivity emerges in PUM-SCs, the first harmonics term I_1 does not vanish owing to the coupling of spin-singlet s-wave superconductivity on both sides of the junctions. Then, since the amplitude of I_1 can be suppressed, φ junctions can be realized. In PUM-SC/PUM-SC Josephson junctions, because even-frequency spin-triplet odd-parity pair amplitudes can be coupled on both sides of the junctions, the current phase relations of the Josephson current can be determined by the edge states of PUM-SCs. In the low transparency limit, the maximum Josephson current can be saturated at low temperature in PUM-SC/spin-singlet s-wave SC junctions. It originates from the coupling of even-frequency spin-singlet even-parity pairings on both sides of the junctions. In PUM-SC/PUM-SC Josephson junctions, the resulting Josephson current I_c clearly depends on the absence or the presence of the edge states. Our findings indicate that the nature of the p-wave superconductivity in PUM-SC is not visible in some Josephson current, owing to the remaining spin-singlet s-wave pairing. However, zero-energy flat bands stemming from the spin-triplet p-wave state can contribute to the Josephson current, and this behavior can be tunable by the chemical potential, which determines the generation of zero-energy flat bands. Our findings indicate that PUM-SCs can be regarded as $s + p$-wave superconductors.

In this work, we have demonstrated the specific situation: p_x-wave and p_y-wave UM, and the chemical potential at $\mu = -4t, -2t$. The presence of zero-energy flat bands caused by the spin-triplet p_x-wave superconductivity mainly plays a role in the current phase relation with higher harmonics and skewness. It indicates that the profile of the current phase relation is determined by the presence or absence of zero-energy flat bands stemming from spin-triplet p_x-wave superconductivity. Indeed, our findings can be applied to generic situations in distinct angles of the PUM Fermi surface tuned by (t_x, t_y) and the chemical potential in PUMs.

In Refs. [123,125], zero-energy flat bands have also been reported by using the other PUM model [71]. Our results have been demonstrated in the PUM model suggested in Ref. [54], and the qualitative results are the same as in Refs. [123,125]. Although the model Hamiltonian and the electronic structure in Refs. [70,71] are different, the noncollinear spin structures that describe the p-wave unconventional magnets are essentially the same. It means that nodal structures shown in Figs. 2(b), 2(c), 3(b), and 3(c) are defined by winding numbers, and these zero-energy flat bands are also topologically protected [15], and we have obtained a similar behavior, even though we have used a simpler model [54]. Hence, the model in Ref. [54] can also capture the essential physics caused

by noncollinear spin structures of p-wave unconventional magnetism, and our conclusion does not change qualitatively, even though we choose a different model Hamiltonian. In addition, we expect that the even-frequency spin-singlet even-parity pair amplitude also coexists with spin-triplet p-wave superconductivity in Refs. [123,125]. Indeed, the Josephson current in our results can also be demonstrated by using the other PUM model [71].

As a future perspective, PUM-SC/PUM/spin-singlet s-wave SC and PUM-SC/PUM/PUM-SC Josephson junctions can be considered to access realistic situations in experiments. Then, since even-frequency spin-singlet even-parity pairings affect the Josephson current, as we demonstrated, the research of s-wave SC/PUM/s-wave SC junctions is needed to unveil the role of p-wave magnetic order. In Ref. [80], the Josephson currents were also obtained in s-wave SC/PUM/s-wave junctions with the simplified PUM model. Thus, adopting effective PUM models [54,71] can support an experimental perspective in Josephson junctions with PUM.

ACKNOWLEDGMENTS

Y.F. acknowledges financial support from the Sumitomo Foundation and the calculation support from Okayama University and Japan Society for the Promotion of Science (JSPS) with Grants-in-Aid for Scientific Research (KAKENHI Grant No. 26K17096). K.Y., Y.F., and Y.T. acknowledge financial support from JSPS with Grants-in-Aid for Scientific Research (KAKENHI Grant No. 25K07203). Y.T. acknowledges financial support from JSPS with Grants-in-Aid for Scientific Research (KAKENHI Grants No. 23K17668, No. 24K00583, No. 24K00556, No. 24K00578, No. 25H00609, and No. 25H00613). We thank B. Lu, J. Cayao, and M. Thakurathi for valuable discussions.

DATA AVAILABILITY

The data that support the findings of this article are not publicly available upon publication because it is not technically feasible and/or the cost of preparing, depositing, and hosting the data would be prohibitive within the terms of this research project. The data are available from the authors upon reasonable request.

APPENDIX A: ENERGY GAP STRUCTURE AND THE EMERGENCE OF NODAL STRUCTURES IN PUM-SCS

We demonstrate the energy gap structure in the bulk and the condition for the emergence of nodal structures of p-wave unconventional magnet/s-wave SC hybrid systems in Appendix A. First of all, we calculate the eigenvalues of the Bogoliubov–de Gennes Hamiltonian. We mentioned that the separated Hamiltonian in the normal state can be obtained as Eq. (2) in Sec. II. Likewise, the Bogoliubov–de Gennes Hamiltonian in Eq. (4) can also be separated into two subspaces $\eta = \pm 1$:

$$\hat{H}^{\eta}_{\mathrm{BdG}}(\boldsymbol{k}) = \varepsilon(\boldsymbol{k})\hat{s}_0 \otimes \hat{\tau}_3 + [t_x \sin k_x + t_y \sin k_y]\hat{s}_3 \otimes \hat{\tau}_0 + \eta J \hat{s}_1 \otimes \hat{\tau}_3 + \Delta i\hat{s}_2 \otimes i\hat{\tau}_2, \tag{A1}$$

with the Pauli matrices in Nambu space $\hat{\tau}_{0,1,2,3}$. By the diagonalization of the above Bogoliubov–de Gennes Hamiltonian, for each sector $\eta = \pm 1$, we obtain the eigenvalues at $t_y = 0$ (p_x-wave UM-SCs),

$$E^{s}_{\pm}(\boldsymbol{k}) = \pm\sqrt{\varepsilon^2(\boldsymbol{k}) + J^2 + t_x^2 \sin^2 k_x + \Delta^2 + 2s\sqrt{\varepsilon^2(\boldsymbol{k})J^2 + \varepsilon^2(\boldsymbol{k})t_x^2 \sin^2 k_x + J^2\Delta^2}}, \tag{A2}$$

with $s = \pm 1$ and

$$\varepsilon(\boldsymbol{k}) = -\mu - 2t\cos k_x - 2t\cos k_y, \tag{A3}$$

and at $t_x = 0$ (p_y-wave UM-SCs):

$$E^{s}_{\pm}(\boldsymbol{k}) = \pm\sqrt{\varepsilon^2(\boldsymbol{k}) + J^2 + t_y^2 \sin^2 k_y + \Delta^2 + 2s\sqrt{\varepsilon^2(\boldsymbol{k})J^2 + \varepsilon^2(\boldsymbol{k})t_y^2 \sin^2 k_y + J^2\Delta^2}}. \tag{A4}$$

Based on these equations, we can find that quasiparticle energy dispersions are doubly degenerate for sectors $\eta = \pm 1$. For the p_x-wave UM-SC $(t_x, t_y) = (t, 0)$, we plot the lowest quasiparticle energy dispersions $E^{-}_{\pm}(\boldsymbol{k})$ on the Fermi surface at $\mu = -4t$ [Fig. 13(a)], and $\mu = -2t$ [Figs. 13(c) and 13(e)], at $J = t$. Then we also show the expectation value of $S_z = (\hbar/2)\hat{s}_z$ ($\langle S_z \rangle$) in the normal state. Point nodes appear at on the k_y axis ($\theta = \pm\pi/2$) with $\langle S_z \rangle = 0$. As well as for p_y-wave UM-SC $(t_x, t_y) = (0, t)$ and $J = t$, we also obtain point nodes on the k_x axis ($\theta = 0, \pi$) and then $\langle S_z \rangle$ vanishes [Figs. 13(b), 13(d), and 13(f)].

Next, we confirm the condition of the emergence of nodal structures in the bulk of PUM-SCs at $(t_x, t_y) = (t, 0)$ (p_x-wave UM-SC), $\mu = -4t$, and $\Delta = 0.01t$. At $J = 0$ [Fig. 14(a)], the fully gapped structure appears. As shown in Fig. 14(b) at $J = 0.005t$, for $J < \Delta$, the energy gap structure is still fully gapped. At $J = \Delta = 0.01t$, the nodal structure is obtained [Fig. 14(c)], and zero-energy flat bands are also realized at $J = 0.02t, 0.10t, 0.50t$ [Figs. 14(d)–14(f)], for $J > \Delta$. Then, in Eq. (A2), we can find the condition of the realization of the gap closing: $J = \Delta$ for $E^{-}_{\pm}(\boldsymbol{k}) = 0$ and $\varepsilon(\boldsymbol{k}) = 0$, at $k_x = 0$. Thus, for $J > \Delta$ with nonzero $t_{x,y}$, nodal structures

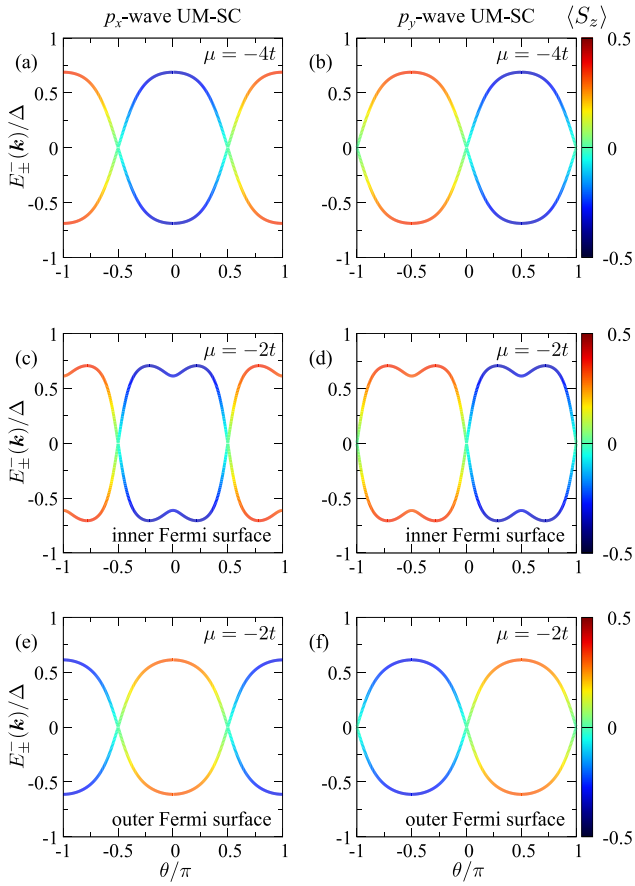


FIG. 13. The lowest quasiparticle energy dispersion $E_{\pm}^{-}(\boldsymbol{k})$ on the Fermi surface, with the expectation values of $\hat{s}_z$ ($\langle S_z \rangle$ in the normal state at (a), (c), (e) $(t_x, t_y) = (t, 0)$ and (b), (d), (f) $(t_x, t_y) = (0, t)$. We select the chemical potential as (a), (b) $\mu = -4t$ and (c)–(f) $\mu = -2t$. θ means the angle in the (k_x, k_y) coordinate. Panels (c) and (d) [(e) and (f)] are for the inner (outer) Fermi surface shown in Figs. 1(d) and 1(f), respectively. Exact nodal points do not appear on the Fermi surface; that is, point nodes misalign from the Fermi surface. Parameters: $J = t$ and $\Delta = 0.01t$.

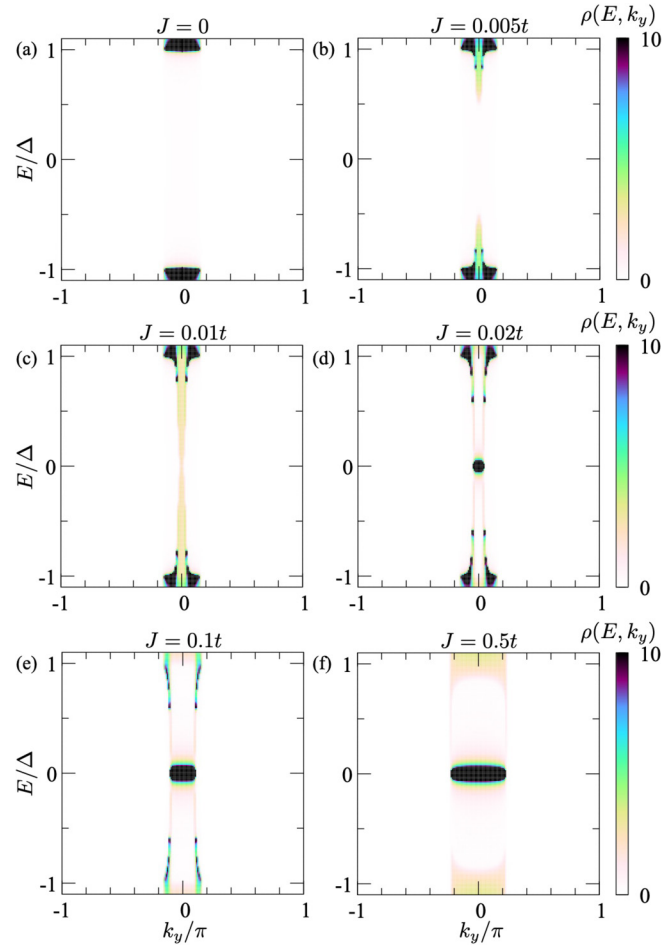


FIG. 14. Momentum-resolved surface density of states at the [100] edge $D(E)$ by changing J at $(t_x, t_y) = (t, 0)$ (p_x-wave UM-SC), $\mu = -4t$, and $\Delta = 0.01t$. We select J as (a) $J = 0$, (b) $J = 0.005t$, (c) $J = 0.01t$, (d) $J = 0.02t$, (e) $J = 0.1t$, and (f) $J = 0.5t$. Nodal structures are formed at $J = \Delta$ in panel (c), and zero-energy flat bands emerge for $J > \Delta$ in panels (d)–(f). Similar behavior is also obtained at $\mu = -2t$.

with zero-energy flat bands can be exhibited in the bulk of PUM-SCs.

APPENDIX B: ANALYTICAL SOLUTION OF THE ANOMALOUS GREEN'S FUNCTIONS OF PUM-SCS IN THE BULK

In Appendix B, we discuss the analytical solution of the anomalous Green's functions (pair amplitude) of PUM-SCs in the bulk. Green's function in the particle-hole Nambu space is calculated as

$$\tilde{G}_\eta(\boldsymbol{k}, i\omega_n) = [i\omega_n - \hat{H}_\eta(\boldsymbol{k})]^{-1} = \begin{pmatrix} \hat{G}(\boldsymbol{k}, i\omega_n) & \hat{F}(\boldsymbol{k}, i\omega_n) \\ \bar{F}(\boldsymbol{k}, i\omega_n) & \bar{G}(\boldsymbol{k}, i\omega_n) \end{pmatrix}, \tag{B1}$$

with the fermionic Matsubara frequency $\omega_n = (2n+1)\pi k_B T$ and the temperature T. When we focus on $(t_x, t_y) = (t, 0)$ (p_x-wave UM), the nonzero pair amplitude is

$$F_{\mathrm{ESE}}^{\uparrow\downarrow}(\boldsymbol{k}, i\omega_n) = -F_{\mathrm{ESE}}^{\downarrow\uparrow}(\boldsymbol{k}, i\omega_n) = \frac{\Delta\left[(\varepsilon(\boldsymbol{k}) - t_x \sin k_x)^2 - J^2 + \omega_n^2 + \Delta^2\right]}{D_x}, \tag{B2}$$

for ESE,

$$F_{\mathrm{ETO}}^{\uparrow\uparrow} = F_{\mathrm{ETO}}^{\downarrow\downarrow} = \frac{2\Delta\eta J t_x \sin k_x}{D_x}, \tag{B3}$$

for ETO,

$$F_{\mathrm{OSO}}^{\uparrow\downarrow}(\boldsymbol{k}, i\omega_n) = F_{\mathrm{OSO}}^{\downarrow\uparrow}(\boldsymbol{k}, i\omega_n) = 0, \tag{B4}$$

for OSO [154,155], and

$$F_{\mathrm{OTE}}^{\uparrow\uparrow} = F_{\mathrm{OTE}}^{\downarrow\downarrow} = \frac{2i\Delta\eta J\omega_n}{D_x}, \tag{B5}$$

for OTE pairings [155–158], with

$$\begin{aligned} D_x =& t_x^4 \sin^4 k_x + \Delta^4 + \varepsilon^4(\boldsymbol{k}) + J^2 \\ & - 2\varepsilon^2(\boldsymbol{k})J^2 + 2\varepsilon^2(\boldsymbol{k})\omega_n^2 + 2J^2\omega_n^2 + \omega_n^4 \\ & + 2\Delta^2\left[\varepsilon^2(\boldsymbol{k}) - J^2 + \omega_n^2\right] \\ & + 2t_x^2 \sin^2 k_x\left[\Delta^2 - \varepsilon^2(\boldsymbol{k}) + J^2 + \omega_n^2\right]. \end{aligned} \tag{B6}$$

As well as at $(t_x, t_y) = (0, t)$ (p_y-wave UM), we obtain

$$\begin{aligned} F_{\mathrm{ESE}}^{\uparrow\downarrow}(\boldsymbol{k}, i\omega_n) &= -F_{\mathrm{ESE}}^{\downarrow\uparrow}(\boldsymbol{k}, i\omega_n) \\ &= \frac{\Delta\left[(\varepsilon(\boldsymbol{k}) - t_y \sin k_y)^2 - J^2 + \omega_n^2 + \Delta^2\right]}{D_y}, \end{aligned} \tag{B7}$$

for ESE,

$$F_{\mathrm{ETO}}^{\uparrow\uparrow}(\boldsymbol{k}, i\omega_n) = F_{\mathrm{ETO}}^{\downarrow\downarrow}(\boldsymbol{k}, i\omega_n) = \frac{2\Delta\eta J t_y \sin k_y}{D_y}, \tag{B8}$$

for ETO,

$$F_{\mathrm{OSO}}^{\uparrow\downarrow}(\boldsymbol{k}, i\omega_n) = F_{\mathrm{OSO}}^{\downarrow\uparrow}(\boldsymbol{k}, i\omega_n) = 0, \tag{B9}$$

for OSO, and

$$F_{\mathrm{OTE}}^{\uparrow\uparrow}(\boldsymbol{k}, i\omega_n) = F_{\mathrm{OTE}}^{\downarrow\downarrow}(\boldsymbol{k}, i\omega_n) = \frac{2i\Delta\eta J\omega_n}{D_y}, \tag{B10}$$

for OTE pairings, with

$$\begin{aligned} D_y =& t_y^4 \sin^4 k_y + \Delta^4 + \varepsilon^4(\boldsymbol{k}) + J^2 \\ & - 2\varepsilon^2(\boldsymbol{k})J^2 + 2\varepsilon^2(\boldsymbol{k})\omega_n^2 + 2J^2\omega_n^2 + \omega_n^4 \\ & + 2\Delta^2\left[\varepsilon^2(\boldsymbol{k}) - J^2 + \omega_n^2\right] \\ & + 2t_y^2 \sin^2 k_y\left[\Delta^2 - \varepsilon^2(\boldsymbol{k}) + J^2 + \omega_n^2\right]. \end{aligned} \tag{B11}$$

Equations (B5) and (B10) indicate that OTE pairing is induced by nonzero J [158]. In addition, to compare with the ESE and ETO pairings, because the denominator is the same in Eqs. (B2) and (B3), we can focus on the numerator to evaluate the sale of the pair amplitude. In Eq. (B2) (ESE pairing), at the Fermi level at $(k_x, k_y) = (k_{\mathrm{F}x}, k_{\mathrm{F}y})$, the scale of $\varepsilon(\boldsymbol{k})$ becomes zero, that is, $\varepsilon(\boldsymbol{k}) \approx 0$. Then, for $t_x = t$, if we do not see the Matsubara frequency term ω_n, the order of the numerator in Eq. (B2) can be approximated as $f_{\mathrm{ESE}} = \Delta(t^2 \sin^2 k_{\mathrm{F}} - J^2 + \Delta^2)$. Likewise, in Eq. (B3) (ETO pairing), for $t_x = t$, we can obtain the scale $f_{\mathrm{ETO}} = 2\Delta J t \sin k_{\mathrm{F}}$. Indeed, the ETO state with equal spins can be dominant in the bulk, not the spin-singlet s wave. We plot f_{ESE} and f_{ETO} as a function of J at Figs. 15(a), $k_{\mathrm{F}x} = 0.4\pi$, and 15(b), $k_{\mathrm{F}x} = 0.0$. We can find $\Delta(t^2 \sin^2 k_{\mathrm{F}} - J^2 + \Delta^2) < 2\Delta J t \sin k_{\mathrm{F}}$ at $k_{\mathrm{F}x} = 0.4\pi$ for $J > 0.4t$ in Fig. 15(a), and then the pair amplitude for ETO pairing becomes larger than ESE pairing. At $k_{\mathrm{F}x} = 0.0$, in Fig. 15(b), f_{ESE} also becomes zero at $J = \Delta$ with $\Delta = 0.01t$, and we obtain $f_{\mathrm{ETO}} = 0$. This corresponds to the formation of the nodal structure at $k_y = 0$ shown in Fig. 14(c). Although we find that nodal structures with zero-energy flat bands appear for $J > \Delta$ discussed in Appendix A, ETO pairing is mainly realized in the bulk by $J > 0.4t$ at $(t_x, t_y) = (t, 0)$.

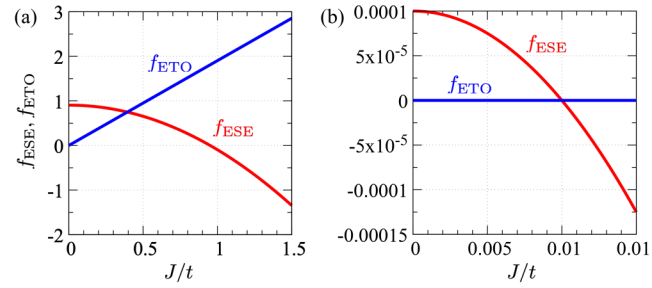


FIG. 15. The value of the numerators $f_{\mathrm{ESE}} = t^2 \sin^2 k_{\mathrm{F}} - J^2 + \Delta^2$ and $f_{\mathrm{ETO}} = 2Jt \sin k_{\mathrm{F}}$ at (a) $k_{\mathrm{F}x} = 0.4\pi$ and (b) $k_{\mathrm{F}x} = 0$, as a function of J. We select the parameters as $t = 1$ and $\Delta = 0.01t$.

APPENDIX C: RECURSIVE GREEN'S FUNCTION METHOD IN JOSEPHSON JUNCTIONS

Here, we provide how we calculate the Josephson current in the present study. We deal with the tight-binding model with the periodic boundary condition along the y direction and semi-infinite SCs on both sides of the junctions shown in Fig. 16. Then we consider the pair potential as $\hat{\Delta}_{\mathrm{L}} = \hat{\Delta}$ on the left and $\hat{\Delta}_{\mathrm{R}} = \hat{\Delta}e^{-i\varphi}$ on the right-side SCs with the phase difference φ.

First of all, for $z = i\omega_n$, we obtain the semi-infinite Green's function in the left $\tilde{G}_{\mathrm{L}}(k_y, i\omega_n)$ and right-side SCs $\tilde{G}_{\mathrm{R}}(k_y, i\omega_n)$; see also Refs. [147,148]. By using the recursive Green's function method [80,147], we calculate the surface Green's function at $j_x = 0, 1$:

$$\tilde{G}_{\mathrm{L}}^{(0)}(k_y, i\omega_n) = [i\omega_n - \tilde{u}_{\mathrm{N}}(k_y) - \tilde{t}_{\mathrm{J}}^{\dagger}\tilde{G}_{\mathrm{L}}(k_y, i\omega_n)\tilde{t}_{\mathrm{J}}]^{-1}, \tag{C1}$$

$$\tilde{G}_{\mathrm{R}}^{(1)}(k_y, i\omega_n) = [i\omega_n - \tilde{u}_{\mathrm{N}}(k_y) - \tilde{t}_{\mathrm{J}}\tilde{G}_{\mathrm{R}}(k_y, i\omega_n)\tilde{t}_{\mathrm{J}}^{\dagger}]^{-1}, \tag{C2}$$

with the local term in the normal metal $\tilde{u}_{\mathrm{N}}(k_y)$. Here, $\tilde{t}_{\mathrm{J}}$ denotes the tunneling Hamiltonian:

$$\tilde{t}_{\mathrm{J}} = t_{\mathrm{int}} \begin{pmatrix} -t & 0 \\ -t & 0 \\ 0 & -t \\ 0 & -t \end{pmatrix} \otimes \hat{\tau}_3, \tag{C3}$$

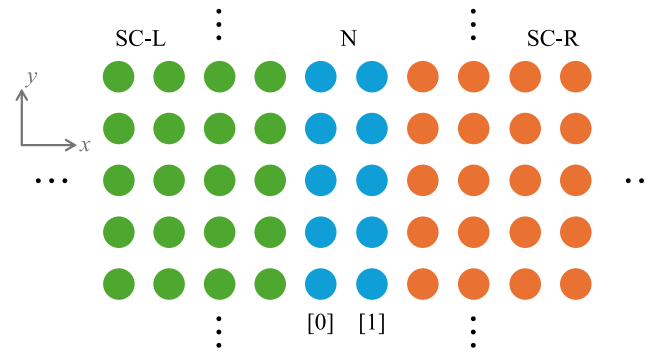


FIG. 16. Schematic illustration of Josephson junctions in the lattice model. SC-L, N, and SC-R indicate the left-side superconductor (SC), the normal metal, and the right-side SC, respectively; [0] and [1] mean the lattice indices along the x direction: $j_x = 0$ and 1, respectively.

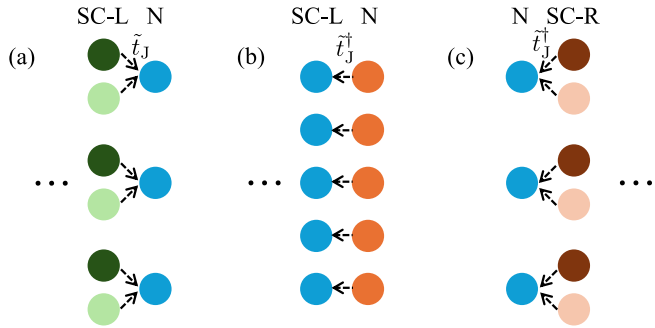


FIG. 17. Schematic illustrations of tunneling processes at the interface for (a) p-wave unconventional magnet (PUM)/s-wave SC hybrid system/normal metal, (b) normal metal/conventional s-wave SC, and (c) normal metal/PUM-SC interfaces. SC-L, N, and SC-R indicate the left-side SC, the normal metal, and the right-side SC, respectively. In (a) and (c), dark and light colors correspond to the sector degrees of freedom in PUM. The black arrows mean the recursive directions for the tunneling Hamiltonian $\tilde{t}_{\rm J}$.

for the PUM-SC/normal metal interface [Fig. 17(a)],

$$\tilde{t}_{\rm J} = t_{\rm int}\begin{pmatrix} -t & 0 \\ 0 & -t \end{pmatrix} \otimes \hat{\tau}_3, \tag{C4}$$

for the normal metal/conventional s-wave SC interface [Fig. 17(b)], and

$$\tilde{t}_{\rm J} = t_{\rm int}\begin{pmatrix} -t & -t & 0 & 0 \\ 0 & 0 & -t & -t \end{pmatrix} \otimes \hat{\tau}_3, \tag{C5}$$

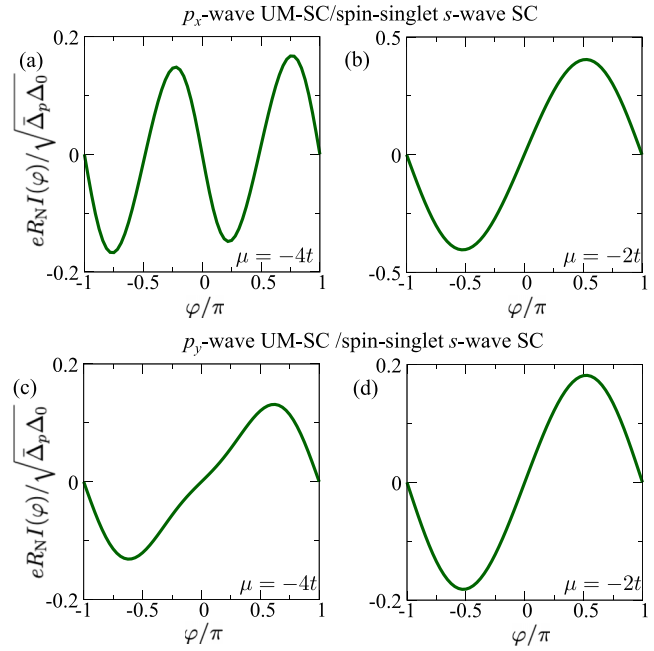


FIG. 18. Current phase relation in PUM-SC/spin-singlet s-wave SC Josephson junctions at (a), (b) $(t_x, t_y) = (t, 0)$ and (c), (d) $(t_x, t_y) = (0, t)$. We select the chemical potential as (a), (c) $\mu = -4t$ and (b), (d) $\mu = -2t$. We choose the critical temperature in PUM-SC as $p = 0.1$. Parameters: $\mu_{\rm N} = -3.5t$, $\mu_s = -1.5t$, $J = t$, $T_{\rm c} = 0.01t$, $T = 0.025T_{\rm c}$, and $t_{\rm int} = 1$.

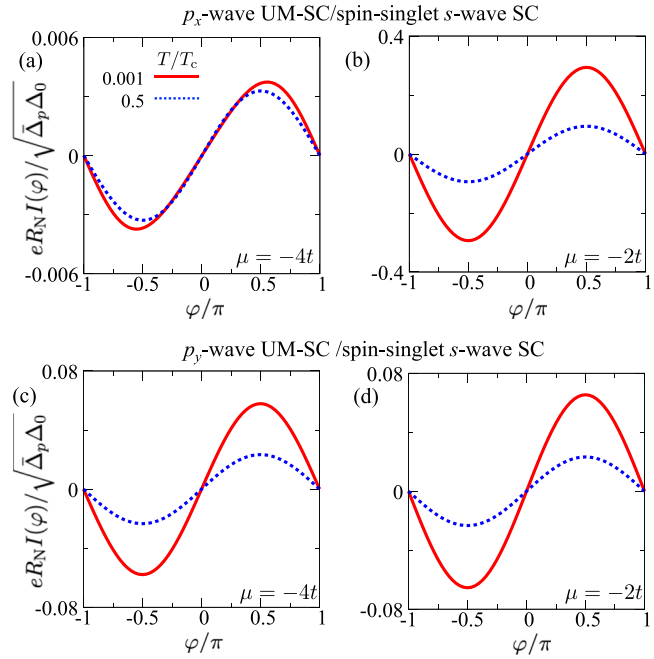


FIG. 19. Current phase relation in PUM-SC/spin-singlet s-wave SC Josephson junctions for $T = 0.001T_{\rm c}$ (red-solid line) and $T = 0.5T_{\rm c}$ (blue-dotted line) at (a), (b) $(t_x, t_y) = (t, 0)$ and (c), (d) $(t_x, t_y) = (0, t)$. We select the chemical potential as (a), (c) $\mu = -4t$ and (b), (d) $\mu = -2t$. We choose the critical temperature in PUM-SC as $p = 0.1$. Parameters: $\mu_{\rm N} = -3.5t$, $\mu_s = -1.5t$, $J = t$, $T_{\rm c} = 0.01t$, $T = 0.025T_{\rm c}$, and $t_{\rm int} = 0.1$.

for the normal metal/PUM-SC interface [Fig. 17(c)], where $t_{\rm int}$ is the transparency amplitude at the interface. In junctions at $j_x = 0, 1$, we obtain the local and nonlocal Green's functions,

$$\tilde{G}_{0,0}(k_y, i\omega_n) = \left[\left\{\tilde{G}_{\rm L}^{(0)}(k_y, i\omega_n)\right\}^{-1} - \tilde{t}_{\rm N}\tilde{G}_{\rm R}^{(1)}(k_y, i\omega_n)\tilde{t}_{\rm N}^{\dagger}\right], \tag{C6}$$

$$\tilde{G}_{1,1}(k_y, i\omega_n) = \left[\left\{\tilde{G}_{\rm R}^{(1)}(k_y, i\omega_n)\right\}^{-1} - \tilde{t}_{\rm N}^{\dagger}\tilde{G}_{\rm L}^{(0)}(k_y, i\omega_n)\tilde{t}_{\rm N}\right], \tag{C7}$$

$$\tilde{G}_{0,1}(k_y, i\omega_n) = \tilde{G}_{\rm L}^{(0)}(k_y, i\omega_n)\tilde{t}_{\rm N}\tilde{G}_{1,1}(k_y, i\omega_n), \tag{C8}$$

$$\tilde{G}_{1,0}(k_y, i\omega_n) = \tilde{G}_{\rm R}^{(1)}(k_y, i\omega_n)\tilde{t}_{\rm N}^{\dagger}\tilde{G}_{0,0}(k_y, i\omega_n), \tag{C9}$$

where $\tilde{t}_{\rm N}$ is the nearest-neighbor hopping term in the normal metal:

$$\tilde{t}_{\rm N} = \begin{pmatrix} -t & 0 \\ 0 & -t \end{pmatrix} \otimes \hat{\tau}_3. \tag{C10}$$

Thus, the Josephson current can be calculated by the nonlocal Green's functions in Eq. (22).

APPENDIX D: JOSEPHSON CURRENT: EFFECT OF THE SMALLER MAGNITUDE OF THE PAIR POTENTIAL IN PUM-SC

Because the effective amplitude of the pair potential in PUM-SC is different from that in spin-singlet s-wave SCs, in Appendix D, we provide the current phase relation when

we choose the smaller magnitude of the pair potential in PUM-SC/spin-singlet s-wave SC Josephson junctions. To analyze the influence of the amplitude of the pair potential in PUM-SC, we demonstrate the Josephson current by choosing $\bar{\Delta}_p = p\Delta_0$ with $p = 0.1$. We plot the current phase relation at the high transparency in PUM-SC/s-wave SC junctions in Fig. 18. We calculate the current phase relation at $p = 0.1$, $T = 0.025T_c$, and $T_c = 0.01t$ in Fig. 18, for each chemical potential at $\mu = -4t$ [Figs. 18(a) and 18(c)] and $\mu = -2t$ [Figs. 18(b) and 18(d)]. Although the amplitude of the maximum Josephson current becomes small, we obtain similar results qualitatively at $p = 0.1$ (Fig. 18), comparing the original results in Figs. 6(b)–6(e). At the low transparency, we show the current phase relation in Fig. 19. The nonsinusoidal feature disappears at $T = 0.001T_c$ and $(t_x, t_y, \mu) = (t, 0, -4t)$ in Fig. 19(a); see also Fig. 9(a). We get similar results qualitatively at $p = 0.1$ [Figs. 19(b)–19(d)], as compared with at $p = 1$ [Figs. 9(b)–9(d)]. Hence, the current phase relations, as well as the temperature dependence, can be influenced by the choice of $\bar{\Delta}_p$.

[1] X.-L. Qi and S.-C. Zhang, Topological insulators and superconductors, Rev. Mod. Phys. **83**, 1057 (2011).

[2] B. A. Bernevig, *Topological Insulators and Topological Superconductors* (Princeton University Press, Princeton, NJ, 2013).

[3] A. P. Schnyder and P. M. Brydon, Topological surface states in nodal superconductors, J. Phys.: Condens. Matter **27**, 243201 (2015).

[4] M. Sato and S. Fujimoto, Majorana fermions and topology in superconductors, J. Phys. Soc. Jpn. **85**, 072001 (2016).

[5] M. Sato and Y. Ando, Topological superconductors: A review, Rep. Prog. Phys. **80**, 076501 (2017).

[6] S. M. Frolov, M. J. Manfra, and J. D. Sau, Topological superconductivity in hybrid devices, Nat. Phys. **16**, 718 (2020).

[7] Y. Tanaka, M. Sato, and N. Nagaosa, Symmetry and topology in superconductors–Odd-frequency pairing and edge states–, J. Phys. Soc. Jpn. **81**, 011013 (2012).

[8] M. Sato, Y. Takahashi, and S. Fujimoto, Non-Abelian topological orders and Majorana fermions in spin-singlet superconductors, Phys. Rev. B **82**, 134521 (2010).

[9] S. D. Sarma, M. Freedman, and C. Nayak, Majorana zero modes and topological quantum computation, npj Quantum Inf. **1**, 15001 (2015).

[10] R. Aguado and L. P. Kouwenhoven, Majorana qubits for topological quantum computing, Phys. Today **73**, 44 (2020).

[11] P. Marra, Majorana nanowires for topological quantum computation, J. Appl. Phys. **132**, 231101 (2022).

[12] C.-R. Hu, Midgap surface states as a novel signature for d^2_{xa}-x^2_b-wave superconductivity, Phys. Rev. Lett. **72**, 1526 (1994).

[13] S. Kashiwaya and Y. Tanaka, Tunnelling effects on surface bound states in unconventional superconductors, Rep. Prog. Phys. **63**, 1641 (2000).

[14] K. Yada, M. Sato, Y. Tanaka, and T. Yokoyama, Surface density of states and topological edge states in noncentrosymmetric superconductors, Phys. Rev. B **83**, 064505 (2011).

[15] M. Sato, Y. Tanaka, K. Yada, and T. Yokoyama, Topology of Andreev bound states with flat dispersion, Phys. Rev. B **83**, 224511 (2011).

[16] P. M. R. Brydon, A. P. Schnyder, and C. Timm, Topologically protected flat zero-energy surface bands in noncentrosymmetric superconductors, Phys. Rev. B **84**, 020501(R) (2011).

[17] Y. Tanaka, S. Tamura, and J. Cayao, Theory of Majorana zero modes in unconventional superconductors, Prog. Theor. Exp. Phys. **2024**, 08C105 (2024).

[18] A. Y. Kitaev, Unpaired Majorana fermions in quantum wires, Phys. Usp. **44**, 131 (2001).

[19] Y. Oreg, G. Refael, and F. von Oppen, Helical liquids and Majorana bound states in quantum wires, Phys. Rev. Lett. **105**, 177002 (2010).

[20] R. M. Lutchyn, J. D. Sau, and S. Das Sarma, Majorana fermions and a topological phase transition in semiconductor-superconductor heterostructures, Phys. Rev. Lett. **105**, 077001 (2010).

[21] M. Leijnse and K. Flensberg, Introduction to topological superconductivity and Majorana fermions, Semicond. Sci. Technol. **27**, 124003 (2012).

[22] R. M. Lutchyn, T. D. Stanescu, and S. Das Sarma, Search for Majorana fermions in multiband semiconducting nanowires, Phys. Rev. Lett. **106**, 127001 (2011).

[23] J. Klinovaja, P. Stano, A. Yazdani, and D. Loss, Topological superconductivity and Majorana fermions in RKKY systems, Phys. Rev. Lett. **111**, 186805 (2013).

[24] P. San-Jose, J. Cayao, E. Prada, and R. Aguado, Multiple Andreev reflection and critical current in topological superconducting nanowire junctions, New J. Phys. **15**, 075019 (2013).

[25] S. Nakosai, Y. Tanaka, and N. Nagaosa, Topological superconductivity in bilayer Rashba system, Phys. Rev. Lett. **108**, 147003 (2012).

[26] H. Ebisu, K. Yada, H. Kasai, and Y. Tanaka, Odd-frequency pairing in topological superconductivity in a one-dimensional magnetic chain, Phys. Rev. B **91**, 054518 (2015).

[27] S. Ikegaya, Y. Asano, and Y. Tanaka, Anomalous proximity effect and theoretical design for its realization, Phys. Rev. B **91**, 174511 (2015).

[28] S. Ikegaya and Y. Asano, Degeneracy of Majorana bound states and fractional Josephson effect in a dirty SNS junction, J. Phys.: Condens. Matter **28**, 375702 (2016).

[29] S. Ikegaya and Y. Asano, Stability of flat zero-energy states at the dirty surface of a nodal superconductor, Phys. Rev. B **95**, 214503 (2017).

[30] S. Ikegaya, S. Kobayashi, and Y. Asano, Symmetry conditions of a nodal superconductor for generating robust flat-band Andreev bound states at its dirty surface, Phys. Rev. B **97**, 174501 (2018).

[31] S. Ikegaya, S. Tamura, D. Manske, and Y. Tanaka, Anomalous proximity effect of planar topological Josephson junctions, Phys. Rev. B **102**, 140505(R) (2020).

[32] S. Ikegaya, J. Lee, A. P. Schnyder, and Y. Asano, Strong anomalous proximity effect from spin-singlet superconductors, Phys. Rev. B **104**, L020502 (2021).

[33] Y. Nagae, A. P. Schnyder, Y. Tanaka, Y. Asano, and S. Ikegaya, Multilocational Majorana zero modes, Phys. Rev. B **110**, L041110 (2024).

[34] Z. Zhu, R. Huang, X. Chen, Z. Cui, X. Duan, J. Zhang, I. Žutić, and T. Zhou, Altermagnetic proximity effect, Phys. Rev. Lett. **136**, 186702 (2026).

[35] Y. Tanaka and S. Kashiwaya, Theory of tunneling spectroscopy of d-wave superconductors, Phys. Rev. Lett. **74**, 3451 (1995).

[36] Y. Tanaka and S. Kashiwaya, Theory of the Josephson effect in d-wave superconductors, Phys. Rev. B **53**, R11957 (1996).

[37] Y. S. Barash, H. Burkhardt, and D. Rainer, Low-temperature anomaly in the Josephson critical current of junctions in d-wave superconductors, Phys. Rev. Lett. **77**, 4070 (1996).

[38] Y. Tanaka and A. A. Golubov, Theory of the proximity effect in junctions with unconventional superconductors, Phys. Rev. Lett. **98**, 037003 (2007).

[39] Y. Tanaka and S. Kashiwaya, Theory of Josephson effects in anisotropic superconductors, Phys. Rev. B **56**, 892 (1997).

[40] Y. Tanaka and S. Kashiwaya, Anomalous charge transport in triplet superconductor junctions, Phys. Rev. B **70**, 012507 (2004).

[41] T. Kokkeler, A. Golubov, F. S. Bergeret, and Y. Tanaka, Full counting statistics for unconventional superconductor junctions, Phys. Rev. B **112**, 024507 (2025).

[42] V. Ambegaokar and A. Baratoff, Tunneling between superconductors, Phys. Rev. Lett. **10**, 486 (1963).

[43] J. A. Pals, W. van Haeringen, and M. H. van Maaren, Josephson effect between superconductors in possibly different spin-pairing states, Phys. Rev. B **15**, 2592 (1977).

[44] E. Fenton, Proximity and Josephson effects for heavy-fermion superconductors, Solid State Commun. **54**, 709 (1985).

[45] E. Fenton, The Josephson effect in superconductors with heavy fermions, Solid State Commun. **60**, 347 (1986).

[46] V. B. Geshkenbein and A. I. Larkin, Pis'ma Zh. Eksp. Teor. Fiz. **43**, 306 (1986).

[47] A. Millis, D. Rainer, and J. A. Sauls, Quasiclassical theory of superconductivity near magnetically active interfaces, Phys. Rev. B **38**, 4504 (1988).

[48] S. Yip, Weak link between conventional and unconventional superconductors, J. Low Temp. Phys. **91**, 203 (1993).

[49] M. Yamashiro, Y. Tanaka, and S. Kashiwaya, Theory of the dc Josephson effect in s-wave/p-wave/s-wave superconductor junction, J. Phys. Soc. Jpn. **67**, 3364 (1998).

[50] Y. Asano, Y. Tanaka, M. Sigrist, and S. Kashiwaya, Josephson current in s-wave-superconductor/Sr_2RuO_4 junctions, Phys. Rev. B **67**, 184505 (2003).

[51] Y. Tanaka, T. Hirai, K. Kusakabe, and S. Kashiwaya, Theory of the Josephson effect in a superconductor/one-dimensional electron gas/superconductor junction, Phys. Rev. B **60**, 6308 (1999).

[52] H.-J. Kwon, K. Sengupta, and V. M. Yakovenko, Fractional ac Josephson effect in p-and d-wave superconductors, Eur. Phys. J. B **37**, 349 (2003).

[53] Y. Asano, Y. Tanaka, and S. Kashiwaya, Anomalous Josephson effect in p-wave dirty junctions, Phys. Rev. Lett. **96**, 097007 (2006).

[54] B. Brekke, P. Sukhachov, H. G. Giil, A. Brataas, and J. Linder, Minimal models and transport properties of unconventional p-wave magnets, Phys. Rev. Lett. **133**, 236703 (2024).

[55] Y. Noda, K. Ohno, and S. Nakamura, Momentum-dependent band spin splitting in semiconducting MnO_2: A density functional calculation, Phys. Chem. Chem. Phys. **18**, 13294 (2016).

[56] M. Naka, S. Hayami, H. Kusunose, Y. Yanagi, Y. Motome, and H. Seo, Spin current generation in organic antiferromagnets, Nat. Commun. **10**, 4305 (2019).

[57] S. Hayami, Y. Yanagi, and H. Kusunose, Momentum-dependent spin splitting by collinear antiferromagnetic ordering, J. Phys. Soc. Jpn. **88**, 123702 (2019).

[58] K.-H. Ahn, A. Hariki, K.-W. Lee, and J. Kuneš, Antiferromagnetism in RuO_2 as d-wave Pomeranchuk instability, Phys. Rev. B **99**, 184432 (2019).

[59] M. Naka, S. Hayami, H. Kusunose, Y. Yanagi, Y. Motome, and H. Seo, Anomalous Hall effect in κ-type organic antiferromagnets, Phys. Rev. B **102**, 075112 (2020).

[60] L.-D. Yuan, Z. Wang, J.-W. Luo, E. I. Rashba, and A. Zunger, Giant momentum-dependent spin splitting in centrosymmetric low-z antiferromagnets, Phys. Rev. B **102**, 014422 (2020).

[61] L. Šmejkal, R. González-Hernández, T. Jungwirth, and J. Sinova, Crystal time-reversal symmetry breaking and spontaneous Hall effect in collinear antiferromagnets, Sci. Adv. **6**, eaaz8809 (2020).

[62] L. Šmejkal, J. Sinova, and T. Jungwirth, Emerging research landscape of altermagnetism, Phys. Rev. X **12**, 040501 (2022).

[63] L. Šmejkal, J. Sinova, and T. Jungwirth, Beyond conventional ferromagnetism and antiferromagnetism: A phase with nonrelativistic spin and crystal rotation symmetry, Phys. Rev. X **12**, 031042 (2022).

[64] I. Mazin, Editorial: Altermagnetism—A new punch line of fundamental magnetism, Phys. Rev. X **12**, 040002 (2022).

[65] L. Bai, W. Feng, S. Liu, L. Šmejkal, Y. Mokrousov, and Y. Yao, Altermagnetism: Exploring new frontiers in magnetism and spintronics, Adv. Funct. Mater. **34**, 2409327 (2024).

[66] C. Song, H. Bai, Z. Zhou, L. Han, H. Reichlova, J. H. Dil, J. Liu, X. Chen, and F. Pan, Altermagnets as a new class of functional materials, Nat. Rev. Mater. **10**, 473 (2025).

[67] I. I. Mazin, Notes on altermagnetism and superconductivity, AAPPS Bull. **35**, 18 (2025).

[68] Y. Fukaya, B. Lu, K. Yada, Y. Tanaka, and J. Cayao, Superconducting phenomena in systems with unconventional magnets, J. Phys.: Condens. Matter **37**, 313003 (2025).

[69] Z. Liu, H. Hu, and X.-J. Liu, Altermagnetism and superconductivity: A short historical review, arXiv:2510.09170.

[70] C. Lee and P. M. R. Brydon, Inversion-asymmetric itinerant antiferromagnets by the space group symmetry, Phys. Rev. Lett. **135**, 116701 (2025).

[71] A. B. Hellenes, T. Jungwirth, R. Jaeschke-Ubiergo, A. Chakraborty, J. Sinova, and L. Šmejkal, P-wave magnets, arXiv:2309.01607.

[72] P. Chatterjee, S. Banik, S. Bera, A. K. Ghosh, S. Pradhan, A. Saha, and A. K. Nandy, Topological superconductivity by engineering noncollinear magnetism in magnet/superconductor heterostructures: A realistic prescription for the two-dimensional Kitaev model, Phys. Rev. B **109**, L121301 (2024).

[73] C. Sun, A. Brataas, and J. Linder, Andreev reflection in altermagnets, Phys. Rev. B **108**, 054511 (2023).

[74] M. Papaj, Andreev reflection at the altermagnet-superconductor interface, Phys. Rev. B **108**, L060508 (2023).

[75] Z. P. Niu and Z. Yang, Orientation-dependent Andreev reflection in an altermagnet/altermagnet/superconductor junction, J. Phys. D **57**, 395301 (2024).
[76] Y. Nagae, A. P. Schnyder, and S. Ikegaya, Spin-polarized specular Andreev reflections in altermagnets, Phys. Rev. B **111**, L100507 (2025).
[77] J. A. Ouassou, A. Brataas, and J. Linder, dc Josephson effect in altermagnets, Phys. Rev. Lett. **131**, 076003 (2023).
[78] C. W. J. Beenakker and T. Vakhtel, Phase-shifted Andreev levels in an altermagnet Josephson junction, Phys. Rev. B **108**, 075425 (2023).
[79] B. Lu, K. Maeda, H. Ito, K. Yada, and Y. Tanaka, φ Josephson junction induced by altermagnetism, Phys. Rev. Lett. **133**, 226002 (2024).
[80] Y. Fukaya, K. Maeda, K. Yada, J. Cayao, Y. Tanaka, and B. Lu, Josephson effect and odd-frequency pairing in superconducting junctions with unconventional magnets, Phys. Rev. B **111**, 064502 (2025).
[81] H.-P. Sun, S.-B. Zhang, C.-A. Li, and B. Trauzettel, Tunable second harmonic in altermagnetic Josephson junctions, Phys. Rev. B **111**, 165406 (2025).
[82] Q. Cheng and Q.-F. Sun, Orientation-dependent Josephson effect in spin-singlet superconductor/altermagnet/spin-triplet superconductor junctions, Phys. Rev. B **109**, 024517 (2024).
[83] W. Zhao, Y. Fukaya, P. Burset, J. Cayao, Y. Tanaka, and B. Lu, Orientation-dependent transport in junctions formed by d-wave altermagnets and d-wave superconductors, Phys. Rev. B **111**, 184515 (2025).
[84] C. Li, J.-X. Hou, F.-C. Zhang, S.-B. Zhang, and L.-H. Hu, Spin-polarized Josephson supercurrent in nodeless altermagnets, Phys. Rev. Lett. **136**, 116701 (2026).
[85] A. Pal, D. Mondal, T. Nag, and A. Saha, Josephson current signature of Floquet Majorana and topological accidental zero modes in altermagnet heterostructures, Phys. Rev. B **112**, L201408 (2025).
[86] S. Banerjee and M. S. Scheurer, Altermagnetic superconducting diode effect, Phys. Rev. B **110**, 024503 (2024).
[87] Q. Cheng, Y. Mao, and Q.-F. Sun, Field-free Josephson diode effect in altermagnet/normal metal/altermagnet junctions, Phys. Rev. B **110**, 014518 (2024).
[88] D. Chakraborty and A. M. Black-Schaffer, Perfect superconducting diode effect in altermagnets, Phys. Rev. Lett. **135**, 026001 (2025).
[89] L. Sharma and M. Thakurathi, Tunable Josephson diode effect in singlet superconductor-altermagnet-triplet superconductor junctions, Phys. Rev. B **112**, 104506 (2025).
[90] D. Debnath, A. Saha, and P. Dutta, Spin polarization and diode effect in thermoelectric current through altermagnet-based superconductor heterostructures, Phys. Rev. B **113**, 104508 (2026).
[91] A. Pal, D. Mondal, T. Nag, and A. Saha, Topological superconductivity and superconducting diode effect mediated via unconventional magnet and Ising spin-orbit coupling, Phys. Rev. B **113**, 195409 (2026).
[92] L. Sharma, B. Ghimire, and M. Thakurathi, p-wave magnet driven field-free Josephson diode effect, arXiv:2602.16677.
[93] S. A. A. Ghorashi, T. L. Hughes, and J. Cano, Altermagnetic routes to Majorana modes in zero net magnetization, Phys. Rev. Lett. **133**, 106601 (2024).
[94] D. Zhu, Z.-Y. Zhuang, Z. Wu, and Z. Yan, Topological superconductivity in two-dimensional altermagnetic metals, Phys. Rev. B **108**, 184505 (2023).
[95] Y.-X. Li and C.-C. Liu, Majorana corner modes and tunable patterns in an altermagnet heterostructure, Phys. Rev. B **108**, 205410 (2023).
[96] Y.-X. Li, Y. Liu, and C.-C. Liu, Creation and manipulation of higher-order topological states by altermagnets, Phys. Rev. B **109**, L201109 (2024).
[97] Y.-X. Li, Realizing tunable higher-order topological superconductors with altermagnets, Phys. Rev. B **109**, 224502 (2024).
[98] D. Mondal, A. Pal, A. Saha, and T. Nag, Distinguishing between topological Majorana and trivial zero modes via transport and shot noise study in an altermagnet heterostructure, Phys. Rev. B **111**, L121401 (2025).
[99] A. Hadjipaschalis, S. A. A. Ghorashi, and J. Cano, Majoranas with a twist: Tunable Majorana zero modes in altermagnetic heterostructures, Phys. Rev. B **112**, 214430 (2025).
[100] T. Hodge, E. Mascot, and S. Rachel, Altermagnet-superconductor heterostructure: A scalable platform for braiding of Majorana modes, arXiv:2506.08095.
[101] O. Alam, A. Pal, P. Dutta, and A. Saha, Proximity-induced superconductivity and emerging topological phases in altermagnet-based heterostructures, arXiv:2510.26894.
[102] B. Fu, C.-A. Li, and B. Trauzettel, Altermagnetism induced Bogoliubov Fermi surfaces form topological superconductivity, arXiv:2512.20049.
[103] G. McArdle, B. Kiraly, P. Wadley, and A. Gammon-Smith, Topological superconductivity in altermagnetic heterostructures on a honeycomb lattice, arXiv:2601.05662.
[104] P. Sharma and N. Mohanta, Double-peak Majorana bound states in altermagnet–superconductor heterostructures, arXiv:2603.25844.
[105] X. Wan, Z. Qin, F. Zhan, J. Zeng, D.-H. Xu, and R. Wang, Chiral superconductivity in periodically driven altermagnet/superconductor heterostructures, arXiv:2604.01596.
[106] S.-B. Zhang, L.-H. Hu, and T. Neupert, Finite-momentum Cooper pairing in proximitized altermagnets, Nat. Commun. **15**, 1801 (2024).
[107] H. G. Giil, B. Brekke, J. Linder, and A. Brataas, Quasiclassical theory of superconducting spin-splitter effects and spin-filtering via altermagnets, Phys. Rev. B **110**, L140506 (2024).
[108] A. A. Zyuzin, Magnetoelectric effect in superconductors with d-wave magnetization, Phys. Rev. B **109**, L220505 (2024).
[109] P. O. Sukhachov, E. W. Hodt, and J. Linder, Thermoelectric effect in altermagnet-superconductor junctions, Phys. Rev. B **110**, 094508 (2024).
[110] P. Sukhachov and J. Linder, Impurity-induced Friedel oscillations in altermagnets and p-wave magnets, Phys. Rev. B **110**, 205114 (2024).
[111] P. Sukhachov, H. G. Giil, B. Brekke, and J. Linder, Coexistence of p-wave magnetism and superconductivity, Phys. Rev. B **111**, L220403 (2025).
[112] K. Maeda, Y. Fukaya, K. Yada, B. Lu, Y. Tanaka, and J. Cayao, Classification of pair symmetries in superconductors with unconventional magnetism, Phys. Rev. B **111**, 144508 (2025).

[113] S. Chourasia, A. Svetogorov, A. Kamra, and W. Belzig, Thermodynamic properties of a superconductor interfaced with an altermagnet, Phys. Rev. B **111**, 224503 (2025).
[114] K. Leraand, K. Mæland, and A. Sudbø, Phonon-mediated spin-polarized superconductivity in altermagnets, Phys. Rev. B **112**, 104510 (2025).
[115] N. Heinsdorf and M. Franz, Proximitizing altermagnets with conventional superconductors, arXiv:2509.03774.
[116] J. Chang, H. Lu, J. Zhao, H.-G. Luo, and Y. Ding, Energy dispersion, superconductivity, and magnetic fluctuations in stacked altermagnetic materials, Phys. Rev. B **111**, 104432 (2025).
[117] K. Monkman, J. Weng, N. Heinsdorf, A. Nocera, and M. Franz, Persistent spin currents in superconducting altermagnets, arXiv:2507.22139.
[118] K. Mukasa and Y. Masaki, Finite-momentum superconductivity in two-dimensional altermagnets with a Rashba-type spin–orbit coupling, J. Phys. Soc. Jpn. **94**, 064705 (2025).
[119] H. Vakili, M. Ali, I. Zutic, and A. A. Kovalev, Supercurrent-driven Néel torque in superconductor/altermagnet hybrids, arXiv:2603.22243.
[120] A. N. Madhusuthanan and M. Karmakar, Thermal stability of pair density wave in a d-wave altermagnetic superconductor, arXiv:2603.25314.
[121] W. Zhao, Y. Fukaya, P. Burset, J. Cayao, Y. Tanaka, and B. Lu, Spin-polarized Josephson current induced by inhomogeneous altermagnetic interlayers, arXiv:2605.02140.
[122] K. Maeda, B. Lu, K. Yada, and Y. Tanaka, Theory of tunneling spectroscopy in unconventional p-wave magnet-superconductor hybrid structures, J. Phys. Soc. Jpn. **93**, 114703 (2024).
[123] Y. Nagae, L. Katayama, and S. Ikegaya, Flat-band zero-energy states and anomalous proximity effects in p-wave magnet–superconductor hybrid systems, Phys. Rev. B **111**, 174519 (2025).
[124] Y. Fukaya, K. Yada, and Y. Tanaka, Tunneling conductance in superconducting junctions with p-wave unconventional magnets breaking time-reversal symmetry, J. Supercond. Nov. Magn. **38**, 228 (2025).
[125] Z.-T. Sun, X. Feng, Y.-M. Xie, B. T. Zhou, J.-X. Hu, and K. T. Law, Pseudo-Ising superconductivity induced by p-wave magnetism, Phys. Rev. B **112**, 214504 (2025).
[126] Q. Song, S. Stavrić, P. Barone, A. Droghetti, D. S. Antonenko, J. W. Venderbos, C. A. Occhialini, B. Ilyas, E. Ergeçen, N. Gedik, *et al.*, Electrical switching of a p-wave magnet, Nature (London) **642**, 64 (2025).
[127] R. Yamada, M. T. Birch, P. R. Baral, S. Okumura, R. Nakano, S. Gao, M. Ezawa, T. Nomoto, J. Masell, Y. Ishihara, *et al.*, A metallic p-wave magnet with commensurate spin helix, Nature (London) **646**, 837 (2025).
[128] J. Linder and J. W. Robinson, Superconducting spintronics, Nat. Phys. **11**, 307 (2015).
[129] B. Lu, P. Mercebach, P. Burset, K. Yada, J. Cayao, Y. Tanaka, and Y. Fukaya, Engineering subgap states in superconductors by the symmetry of altermagnetism, Phys. Rev. B **113**, L180501 (2026).
[130] Y. Fukaya, B. Lu, K. Yada, Y. Tanaka, and J. Cayao, Crossed surface flat bands in three-dimensional superconducting altermagnets, Phys. Rev. Lett. **136**, 226001 (2026).
[131] M. Khodas, L. Šmejkal, and I. I. Mazin, Nonrelativistic-Ising superconductivity in p-wave magnets, arXiv:2601.19829.
[132] A. Pal, P. Dutta, and A. Saha, Emergent superconducting phases in unconventional p-wave magnets: Topological superconductivity, Bogoliubov Fermi surfaces and superconducting diode effect, arXiv:2603.03221.
[133] X.-J. Luo, Z.-T. Sun, X. Feng, M. Tian, and K. T. Law, Hidden Zeeman field in odd-parity magnets: An ideal platform for topological superconductivity, arXiv:2603.15147.
[134] K.-M. Kim, G. Sim, and M. J. Park, Topological Ising superconductivity in two-dimensional p-wave magnet, arXiv:2605.01686.
[135] X.-J. Yi, Y. Mao, P.-Y. Liu, Y.-F. Sun, and Q.-F. Sun, Spin-triplet pairing and spin supercurrent in p-wave magnetic superconductors, Phys. Rev. B **113**, 214511 (2026).
[136] K. Bera, P. Mohan, and A. Saha, Generation and time evolution of anomalous Floquet Majorana flat edge modes in two-dimensional noncolinear magnet-superconductor heterostructures, arXiv:2606.03193.
[137] D. Liu, Z.-Y. Zhuang, D. Zhu, Z. Wu, and Z. Yan, Nonrelativistic spin-orbit-coupling effects in odd-parity coplanar magnets, arXiv:2606.23806.
[138] B. A. Bernevig, J. Orenstein, and S.-C. Zhang, Exact SU(2) symmetry and persistent spin helix in a spin-orbit coupled system, Phys. Rev. Lett. **97**, 236601 (2006).
[139] M. Kohda, V. Lechner, Y. Kunihashi, T. Dollinger, P. Olbrich, C. Schönhuber, I. Caspers, V. V. Bel'kov, L. E. Golub, D. Weiss, K. Richter, J. Nitta, and S. D. Ganichev, Gate-controlled persistent spin helix state in (In,Ga)As quantum wells, Phys. Rev. B **86**, 081306(R) (2012).
[140] X. Liu, J. K. Jain, and C.-X. Liu, Long-range spin-triplet helix in proximity induced superconductivity in spin-orbit-coupled systems, Phys. Rev. Lett. **113**, 227002 (2014).
[141] S. H. Jacobsen, J. A. Ouassou, and J. Linder, Critical temperature and tunneling spectroscopy of superconductor-ferromagnet hybrids with intrinsic Rashba-Dresselhaus spin-orbit coupling, Phys. Rev. B **92**, 024510 (2015).
[142] F. Yang and M. W. Wu, Gapped superconductivity with all symmetries in InSb (110) quantum wells in proximity to s-wave superconductor in Fulde-Ferrell-Larkin-Ovchinnikov phase or with a supercurrent, Phys. Rev. B **95**, 075304 (2017).
[143] M. Alidoust, Critical supercurrent and φ_0 state for probing a persistent spin helix, Phys. Rev. B **101**, 155123 (2020).
[144] M. Alidoust, C. Shen, and I. Žutić, Cubic spin-orbit coupling and anomalous Josephson effect in planar junctions, Phys. Rev. B **103**, L060503 (2021).
[145] J. Lee, S. Ikegaya, and Y. Asano, Odd-parity pairing correlations in a d-wave superconductor, Phys. Rev. B **103**, 104509 (2021).
[146] A. M. Black-Schaffer and S. Doniach, Self-consistent solution for proximity effect and Josephson current in ballistic graphene SNS Josephson junctions, Phys. Rev. B **78**, 024504 (2008).
[147] A. Umerski, Closed-form solutions to surface Green's functions, Phys. Rev. B **55**, 5266 (1997).
[148] D. Takagi, S. Tamura, and Y. Tanaka, Odd-frequency pairing and proximity effect in Kitaev chain systems including a topological critical point, Phys. Rev. B **101**, 024509 (2020).

[149] Y. Tanuma, K. Kuroki, Y. Tanaka, R. Arita, S. Kashiwaya, and H. Aoki, Determination of pairing symmetry from magnetotunneling spectroscopy: A case study for quasi-one-dimensional organic superconductors, Phys. Rev. B **66**, 094507 (2002).

[150] K. Sengupta, I. Žutić, H.-J. Kwon, V. M. Yakovenko, and S. Das Sarma, Midgap edge states and pairing symmetry of quasi-one-dimensional organic superconductors, Phys. Rev. B **63**, 144531 (2001).

[151] Y. Tanaka, A. A. Golubov, S. Kashiwaya, and M. Ueda, Anomalous Josephson effect between even- and odd-frequency superconductors, Phys. Rev. Lett. **99**, 037005 (2007).

[152] Y. Tanaka, Y. Tanuma, and A. A. Golubov, Odd-frequency pairing in normal-metal/superconductor junctions, Phys. Rev. B **76**, 054522 (2007).

[153] S. Tamura, S. Hoshino, and Y. Tanaka, Odd-frequency pairs in chiral symmetric systems: Spectral bulk-boundary correspondence and topological criticality, Phys. Rev. B **99**, 184512 (2019).

[154] A. Balatsky and E. Abrahams, New class of singlet superconductors which break the time reversal and parity, Phys. Rev. B **45**, 13125 (1992).

[155] J. Linder and A. V. Balatsky, Odd-frequency superconductivity, Rev. Mod. Phys. **91**, 045005 (2019).

[156] V. Berezinskii, New model of the anisotropic phase of superfluid He3, JETP Lett. **20**, 287 (1974).

[157] T. R. Kirkpatrick and D. Belitz, Disorder-induced triplet superconductivity, Phys. Rev. Lett. **66**, 1533 (1991).

[158] F. S. Bergeret, A. F. Volkov, and K. B. Efetov, Odd triplet superconductivity and related phenomena in superconductor-ferromagnet structures, Rev. Mod. Phys. **77**, 1321 (2005).

[159] K. Kawai, K. Yada, Y. Tanaka, Y. Asano, A. A. Golubov, and S. Kashiwaya, Josephson effect in a multiorbital model for Sr_2RuO_4, Phys. Rev. B **95**, 174518 (2017).

[160] Y. Fukaya, K. Yada, Y. Tanaka, P. Gentile, and M. Cuoco, Orbital tunable $0-\pi$ transitions in Josephson junctions with noncentrosymmetric topological superconductors, Phys. Rev. B **102**, 144512 (2020).

[161] T. Sakamori, S. Kashiwaya, R. Yano, Y. Tanaka, T. Hatano, and K. Yada, Theory of Josephson current on a lattice model of grain boundary in d-wave superconductors, Supercond. Sci. Technol. **36**, 085011 (2023).

[162] Y. Fukaya, Y. Tanaka, P. Gentile, K. Yada, and M. Cuoco, Anomalous Josephson coupling and high-harmonics in non-centrosymmetric superconductors with s-wave spin-triplet pairing, npj Quantum Mater. **7**, 99 (2022).

[163] A. A. Golubov, M. Y. Kupriyanov, and E. Il'ichev, The current-phase relation in Josephson junctions, Rev. Mod. Phys. **76**, 411 (2004).

[164] I. O. Kulik and A. N. Omelyanchuk, Josephson effect in superconductive bridges: Microscopic theory, Sov. J. Low Temp. Phys. **4**, 142 (1978).

[165] W. L. McMillan, Tunneling model of the superconducting proximity effect, Phys. Rev. **175**, 537 (1968).

[166] N. G. Pugach, E. Goldobin, R. Kleiner, and D. Koelle, Method for reliable realization of a φ Josephson junction, Phys. Rev. B **81**, 104513 (2010).

[167] B. Braunecker, G. I. Japaridze, J. Klinovaja, and D. Loss, Spin-selective Peierls transition in interacting one-dimensional conductors with spin-orbit interaction, Phys. Rev. B **82**, 045127 (2010).

[168] S. Nakosai, Y. Tanaka, and N. Nagaosa, Two-dimensional *p*-wave superconducting states with magnetic moments on a conventional *s*-wave superconductor, Phys. Rev. B **88**, 180503(R) (2013).

[169] I. Martin and A. F. Morpurgo, Majorana fermions in superconducting helical magnets, Phys. Rev. B **85**, 144505 (2012).

[170] S. Nadj-Perge, I. K. Drozdov, B. A. Bernevig, and A. Yazdani, Proposal for realizing Majorana fermions in chains of magnetic atoms on a superconductor, Phys. Rev. B **88**, 020407(R) (2013).